IQGAP1 suppresses TβRII-mediated myofibroblastic activation and metastatic growth in liver

Chunsheng Liu,[1] Daniel D. Billadeau,[2] Haitham Abdelhakim,[1] Edward Leof,[3] Kozo Kaibuchi,[4] Carmelo Bernabeu,[5] George S. Bloom,[6] Liu Yang,[1] Lisa Boardman,[1] Vijay H. Shah,[1] and Ningling Kang[1]

[1]GI Research Unit and Cancer Cell Biology Program, [2]Department of Immunology, and [3]Thoracic Diseases Research Unit, Mayo Clinic, Rochester, Minnesota, USA. [4]Department of Cell Pharmacology, Nagoya University Graduate School of Medicine, Nagoya, Japan. [5]Centro de Investigaciones Biologicas, Consejo Superior de Investigaciones Cientificas (CSIC), and Centro de Investigacion Biomedica en Red de Enfermedades Raras (CIBERER), Madrid, Spain. [6]Department of Biology and Cell Biology, University of Virginia, Charlottesville, Virginia, USA.

In the tumor microenvironment, TGF-β induces transdifferentiation of quiescent pericytes and related stromal cells into myofibroblasts that promote tumor growth and metastasis. The mechanisms governing myofibroblastic activation remain poorly understood, and its role in the tumor microenvironment has not been explored. Here, we demonstrate that IQ motif containing GTPase activating protein 1 (IQGAP1) binds to TGF-β receptor II (TβRII) and suppresses TβRII-mediated signaling in pericytes to prevent myofibroblastic differentiation in the tumor microenvironment. We found that TGF-β1 recruited IQGAP1 to TβRII in hepatic stellate cells (HSCs), the resident liver pericytes. *Iqgap1* knockdown inhibited the targeting of the E3 ubiquitin ligase SMAD ubiquitination regulatory factor 1 (SMURF1) to the plasma membrane and TβRII ubiquitination and degradation. Thus, *Iqgap1* knockdown stabilized TβRII and potentiated TGF-β1 transdifferentiation of pericytes into myofibroblasts in vitro. *Iqgap1* deficiency in HSCs promoted myofibroblast activation, tumor implantation, and metastatic growth in mice via upregulation of paracrine signaling molecules. Additionally, we found that IQGAP1 expression was downregulated in myofibroblasts associated with human colorectal liver metastases. Taken together, our studies demonstrate that IQGAP1 in the tumor microenvironment suppresses TβRII and TGF-β dependent myofibroblastic differentiation to constrain tumor growth.

Introduction

Cells within the tumor microenvironment are increasingly recognized as critical determinants for tumor growth (1–4). In this regard, TGF-β–mediated activation of pericytes and other mesenchymal stromal cells into tumor-associated myofibroblasts promotes a metastatic tumor microenvironment by increasing growth factor–induced angiogenesis, desmoplastic matrix, and tumor stiffness (2–4). Thus, mechanisms that regulate TGF-β signaling in cells undergoing myofibroblastic activation are critical to better understanding and targeting the tumor microenvironment and tumor growth.

The effects of TGF-β1 on cells are mediated by the formation of a heteromeric complex on the plasma membrane that contains 2 receptors: TGF-β receptor I (TβRI) and TβRII (5, 6). Upon TGF-β1 stimulation, TβRII recruits and activates TβRI by phosphorylating TβRI at Glycine-Serine domains. Subsequently, active TβRI interacts and phosphorylates SMAD2 and SMAD3, which oligomerize with SMAD4. The SMAD complexes then translocate into the nucleus, where they collaborate with other transcription factors to regulate gene expression such as α-SMA and fibronectin, markers of myofibroblastic activation (6).

IQ motif containing GTPase activating protein 1 (IQGAP1) is a large protein that regulates diverse cellular functions by interacting with more than 90 proteins (7–10). IQGAP1 controls cellular protrusions, cell shape, and motility by regulating dynamics of actin and microtubule (11–13). Additionally, it promotes cell proliferation (14, 15), reduces cell-cell adhesions and increases migration (16), interacts with β-catenin, and modulates β-catenin–mediated transcription (16, 17). Finally, IQGAP is also an MAPK scaffold (18).

IQGAP1 is currently proposed as an oncogenic protein in epithelial cells that may promote tumorigenesis and metastasis (7, 8, 14). However, *Iqgap1*-knockout mice exhibit an increase in late-onset gastric hyperplasia as compared with wild-type mice (19), implying a complex role of IQGAP1 in tumor growth. It is conceivable that IQGAP1 may exert different functions depending on the presence of binding partners and on the nature of cells. Moreover, the role of IQGAP1 in myofibroblastic activation in the tumor microenvironment remains entirely unexplored. Recent descriptions that IQGAP1 binds to receptors of VEGF, FGF, and EGF (13, 20, 21) and links growth factor signaling to the actin cytoskeleton prompted us to explore a potential role for IQGAP in the regulation of TGF-β receptors and their signaling in mesenchymal-type cells that activate into tumor-associated myofibroblasts, such as hepatic stellate cells (HSCs) (22), which are resident liver pericytes.

Here, we report that the C-terminal aa 1503–1657 region of IQGAP1 binds to TβRII and that IQGAP1/TβRII binding is required for suppressing TβRII and TGF-β signaling in primary human HSCs. IQGAP1 is required for the targeting of the E3 ubiquitin ligase SMAD ubiquitination regulatory factor 1 (SMURF1)

Conflict of interest: The authors have declared that no conflict of interest exists.
Citation for this article: *J Clin Invest.* 2013;123(3):1138–1156. doi:10.1172/JCI63836.

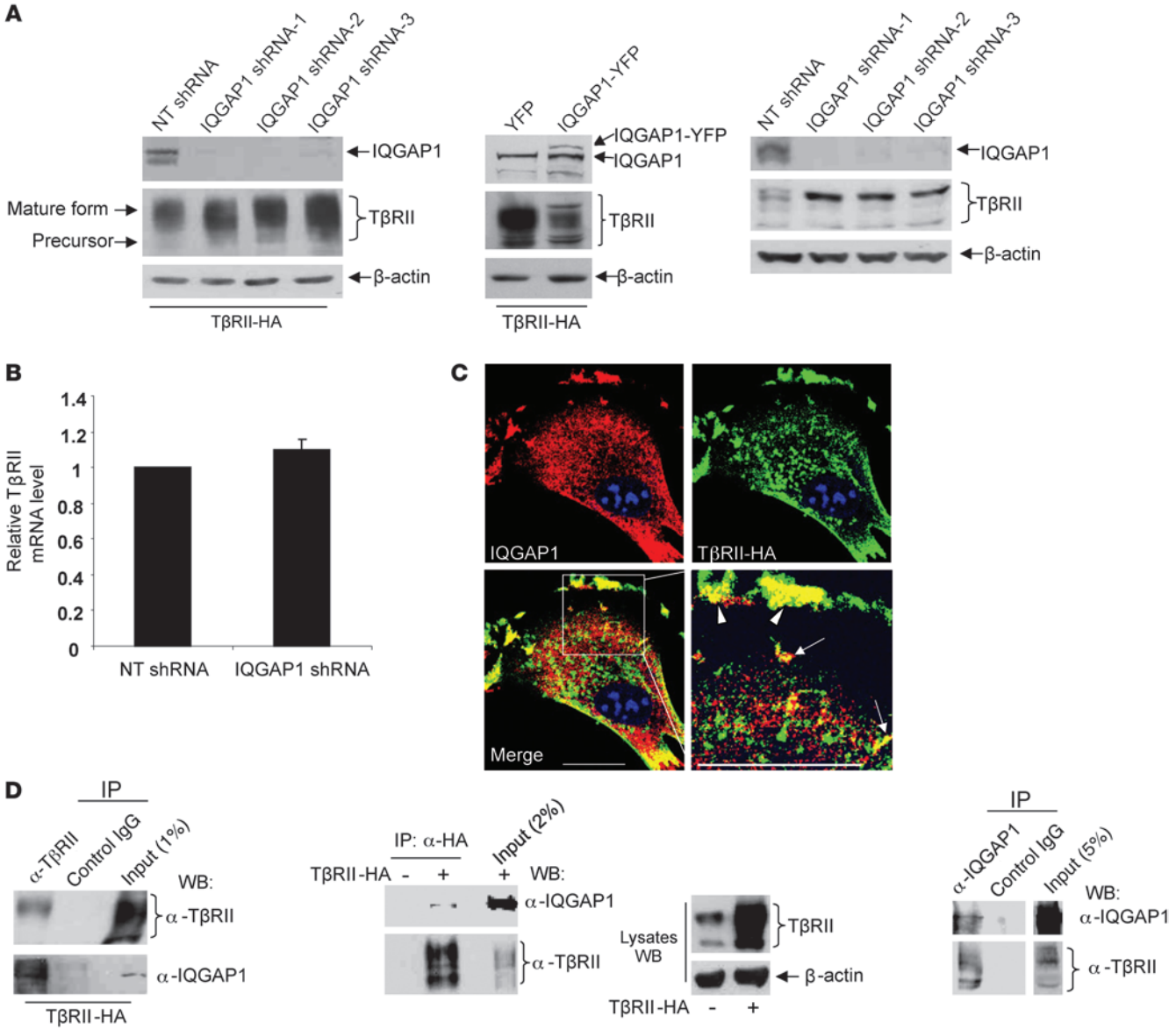

Figure 1

IQGAP1 interacts with TβRII and regulates its stability. (**A**) Left: HSCs that express TβRII-HA by retroviral transduction were transduced with lentiviruses encoding nontargeting shRNA (NT shRNA, control) or IQGAP1 shRNAs, and subjected to WB for TβRII. Knockdown of IQGAP1 by 3 different shRNAs consistently upregulated TβRII protein levels. Middle: cells were transduced with retroviruses encoding YFP (control) or IQGAP1-YFP. Overexpression of IQGAP in HSCs reduced TβRII protein. Right: endogenous TβRII protein levels increased in IQGAP1-knockdown cells. (**B**) HSCs transduced with lentiviruses encoding either NT shRNA or IQGAP1 shRNA were harvested for RNA extraction and SYBR green–based real-time RT-PCR. IQGAP1 knockdown did not change *TβRII* mRNA levels. $n = 3$ independent experiments. (**C**) IQGAP1 (red) and TβRII-HA (green) colocalized at the plasma membrane (arrowheads) and in intracellular vesicles (arrows) in HSCs by IF. Scale bars 20 μm. (**D**) Left: TβRII coprecipitated with IQGAP1 when IP was performed using anti-IQGAP1. Middle: IQGAP1 coprecipitated with TβRII-HA when IP was performed using anti-HA. Right: IQGAP1 coprecipitated with endogenous TβRII when IP was performed using anti-TβRII. Data are representative of multiple repeats with similar results.

to the plasma membrane and TβRII ubiquitination. IQGAP1 of HSCs suppresses myofibroblastic activation and tumor growth in mice and IQGAP1 in the myofibroblasts of human colorectal liver metastases is downregulated. Thus, our data demonstrate a new role for stromal IQGAP1 in the suppression of TGF-β–mediated activation of quiescent pericytes into myofibroblasts in the tumor microenvironment.

Results

IQGAP1 regulates TβRII abundance in HSCs. Since TβRII is the most upstream receptor that initiates TGF-β signaling, we tested to determine whether IQGAP1 associated with TβRII and regulated TβRII in human primary HSCs (23). To this end, we first validated the specificity of anti-TβRII antibody by Western blot (WB) analyses, since the quality of commercial anti-TβRII is vari-

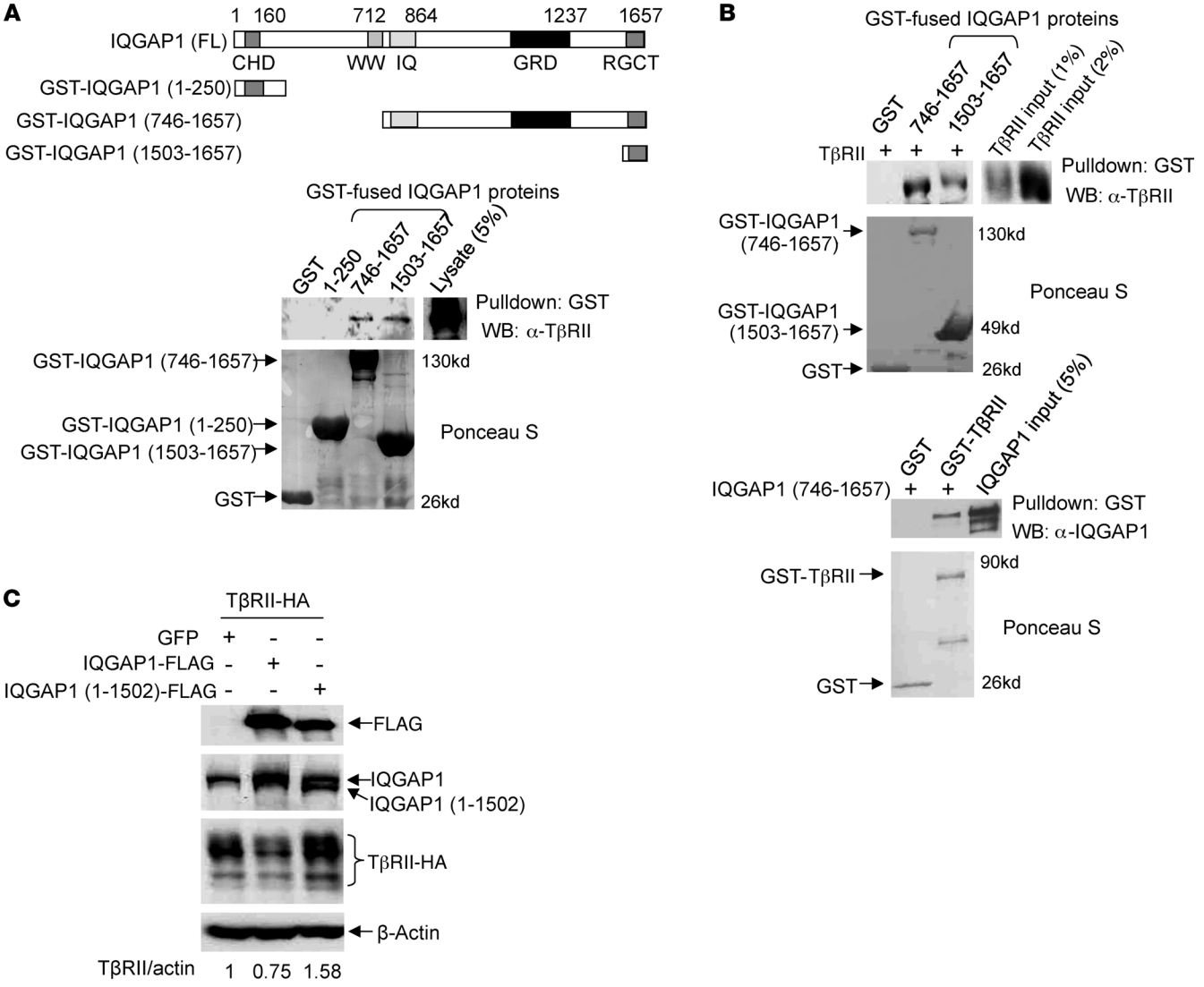

Figure 2

IQGAP1 C terminus aa 1503–1657 is required for binding and suppressing TβRII. (**A**) Top 4 rows: full-length (FL) IQGAP1 and GST-fused truncated IQGAP1 proteins are shown. Bottom, GST fused truncated IQGAP1 proteins extracted from bacteria were incubated with HSC lysates for GST pull-down assays. Both aa 746–1657 and aa 1503–1657 of IQGAP1 bound to TβRII. Ponceau S staining depicted the purity of the recombinant proteins. (**B**) Top: after the GST tag of GST-TRII was removed by thrombin treatment, detagged TβRII was incubated with GST-fused IQGAP1 proteins for in vitro binding assays. Both aa 746–1657 and aa 1503–1657 of IQGAP1 bound to TβRII directly in vitro. Ponceau S staining depicted the purity of GST and GST-fused IQGAP1 proteins. Bottom: detagged IQGAP1 aa 746–1657 was incubated with GST or GST-TβRII for in vitro binding assays. GST-TβRII bound to IQGAP1 aa 746-1657 directly in vitro. aa 746–1657 instead of aa 1503–1657 of IQGAP1 was used in this assay because IQGAP1 antibodies could not recognize aa 1503–1657 of IQGAP1. Ponceau S staining depicted the purity of GST and GST fusion proteins. (**C**) HSCs expressing TβRII-HA were transduced with lentiviruses encoding GFP, IQGAP1-FLAG, or IQGAP1 (1-1502)-FLAG, and subjected to WB. In contrast with IQGAP1, IQGAP1 (1-1502) mutant lacking the TβRII binding region failed to repress TβRII protein levels. Densitometric ratios are shown on the bottom. All data shown represent multiple repeats with similar results.

able (Supplemental Figure 1; supplemental material available online with this article; doi:10.1172/JCI63836DS1). Using this antibody, we found that IQGAP1 regulates TRII abundance in HSCs (Figure 1A). To avoid the possibility of off-target effects of shRNA, multiple IQGAP1 shRNAs (Sigma-Aldrich), each targeting a distinct sequence of human IQGAP1, were used to knock down IQGAP1. In cells expressing TβRII-HA, IQGAP1 knockdown increased TβRII protein levels and overexpression of IQGAP1 decreased TβRII (Figure 1A). Additionally, IQGAP1 shRNAs also increased endogenous TβRII protein levels (Figure 1A). Thus, *Iqgap1* activity reduces levels of TβRII protein in HSCs.

IQGAP1 interacts with TβRII in HSCs. Quantitative real-time RT-PCR revealed that IQGAP1 knockdown did not influence *TβRII* mRNA levels (Figure 1B), suggesting that IQGAP1 regulates TβRII stability at the posttranscriptional level, possibly by binding to TβRII and promoting its degradation. To test this hypothesis, we

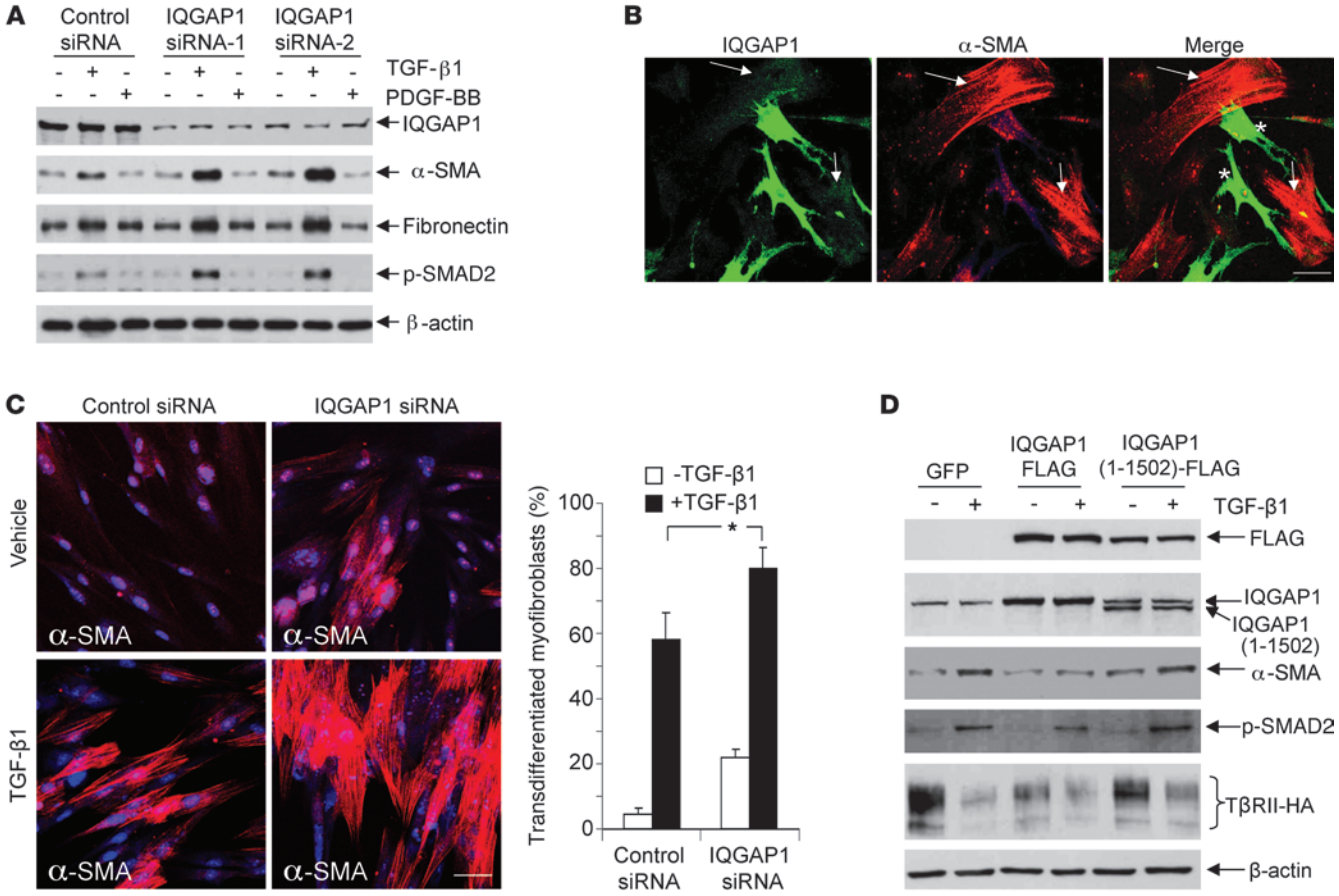

Figure 3

IQGAP1 suppresses TGF-β–mediated activation of HSCs into myofibroblasts. (**A**) HSCs that were transfected with control or IQGAP1 siRNA were serum-starved and stimulated with TGF-β1 (5 ng/ml) or PDGF-BB (20 ng/ml). HSC activation was assessed by WB for activation markers such as α-SMA, fibronectin, and p-SMAD2. TGF-β1 but not PDGF-BB induced upregulation of α-SMA and fibronectin. Two different IQGAP1 siRNAs consistently potentiated the effect of TGF-β1. (**B**) HSCs that were transfected with IQGAP1 siRNA were mixed with control cells for double IF for IQGAP1 (green) and α-SMA (red). As compared with nontransfected HSCs (asterisks), IQGAP1 knockdown induced the formation of α-SMA–positive stress fibers (arrows), indicative of myofibroblastic transdifferentiation of HSCs. Scale bar: 50 μm. (**C**) Left: HSCs treated as described in **A** were subjected to IF for α-SMA. TGF-β1 promoted the formation of α-SMA–positive stress fibers, and this effect was potentiated by IQGAP1 siRNA. Scale bar: 50 μm. Right: quantitative data of α-SMA IF showing that IQGAP1 knockdown significantly increased TGF-β1 activation of HSCs into myofibroblasts. *$P < 0.05$ by ANOVA. $n = 7$ randomly picked microscopic fields, each containing 100–200 cells. (**D**) HSCs that express GFP, IQGAP1-FLAG, or IQGAP1 (1-1502)-FLAG were stimulated with TGF-β1 and harvested for WB. IQGAP1 downregulated TβRII and inhibited HSC activation. In contrast, IQGAP1 (1-1502) mutant failed to suppress TβRII and TGF-β signaling. Data represent 3 independent experiments with similar results.

performed double immunofluorescence staining (IF) for IQGAP1 and TβRII and found that IQGAP1 and TβRII colocalized at the peripheral plasma membrane (arrowheads, Figure 1C) and in endocytic vesicles (arrows, Figure 1C) in cells expressing TβRII-HA. Coimmunoprecipitation (IP) also demonstrated that these 2 proteins coprecipitated in HSCs expressing TβRII-HA (Figure 1D). Furthermore, IQGAP coprecipitated with endogenous TβRII from cells as well (Figure 1D). These data suggest that IQGAP1 interacts with TβRII in HSCs. Additionally, the interactions between these 2 proteins occur in other cell types as well (Supplemental Figure 5).

IQGAP1 aa 1503–1657 is required for binding and suppressing TRII. IQGAP1 contains multiple protein-protein interacting domains including calponin-homology domain (CHD), poly-proline protein-protein domain (WW), IQ domain (IQ), Ras GTPase-activating protein–related domain (GRD), and RasGAP C terminus (RGCt) (Figure 2A and ref. 9). So we performed in vitro glutathione-*S*-transferase (GST) pull-down assays to map the TβRII-binding region on IQGAP1. Both aa 746–1657 and aa 1503–1657 of IQGAP1 interacted with TβRII by GST pull-down assays (Figure 2A), suggesting that the TβRII-binding region is within the smaller C-terminal 1503–1657 fragment. To understand whether IQGAP1/TβRII binding is direct or requires adaptor proteins, we performed in vitro protein-binding assays by incubating detagged TβRII (the GST tag was removed by thrombin) with GST-fused IQGAP1 proteins (Figure 2B), or detagged IQGAP1 with GST-fused TβRII (Figure 2B and Supplemental Figure 2). Both experiments demonstrated a direct binding of these 2 proteins in vitro.

To test the role of aa 1503–1657 of IQGAP1 in IQGAP1/TβRII binding and TβRII abundance, we generated a IQGAP1 (1-1502) mutant that lacks aa 1503–1657 and found that this mutant failed to suppress

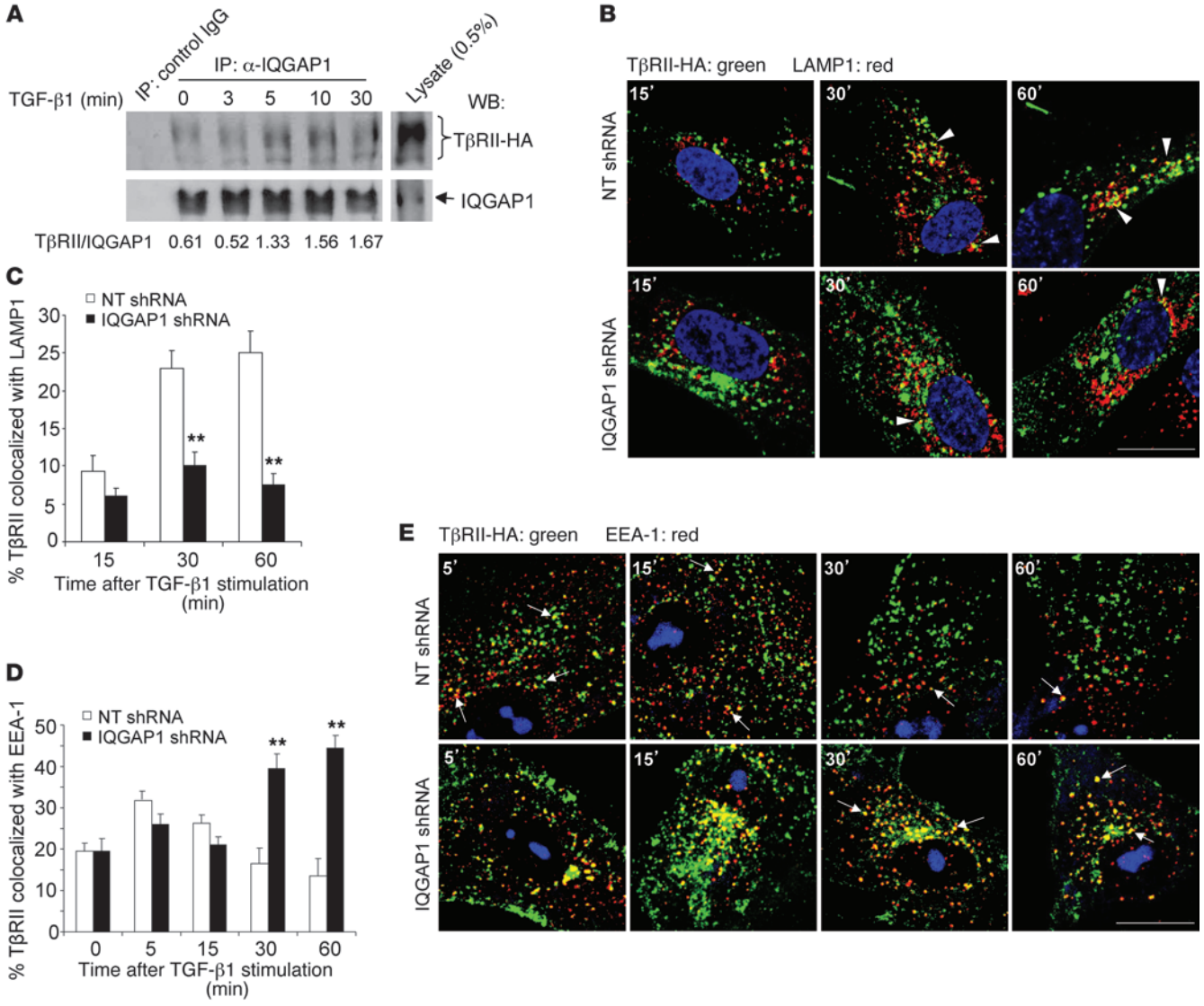

Figure 4

TGF-β1 increases IQGAP1/TβRII binding, and IQGAP1 knockdown inhibits lysosomal targeting of TβRII. (**A**) HSCs that express TβRII-HA were serum starved and stimulated with TGF-β1 for indicated times. Cell lysates were subjected to IP using anti-IQGAP1, and coprecipitated TβRII was detected by WB. Densitometric ratios are shown on the bottom. TGF-β1 increased IQGAP1/TβRII binding. Blots represent 3 independent experiments. (**B** and **C**) HSCs that were serum starved and pretreated with cycloheximide (40 μg/ml) for 1 hour were incubated with TGF-β1 at 4°C for ligand/receptor binding. After cells were incubated at 37°C for indicated times, cells were fixed for double IF for HA (green) and LAMP1 (red). IQGAP1 knockdown significantly reduced TβRII in late endosome/lysosomes at both 30 and 60 minutes after TGF-β1 stimulation (arrowheads). Scale bar: 20 μm. $^{**}P < 0.01$ by ANOVA. $n = 6$ cells each group. Data represent 3 independent experiments with identical results. (**D** and **E**) Cells treated as described in **B** and **C** were stained for HA and EEA-1. IQGAP1 knockdown induced the accumulation of TβRII in EEA-1–positive endosomes at both 30 and 60 minutes after TGF-β1 stimulation (arrows). Scale bar: 20 μm. $^{**}P < 0.01$ by ANOVA. $n = 6$ cells each group. Data are representative of 3 independent repeats with identical results.

TβRII protein levels in contrast with full-length IQGAP1 (Figure 2C). Thus, IQGAP1 aa 1503–1657 is required for IQGAP1/TβRII binding and suppressing TβRII. Interestingly, the C-terminal region of IQGAP has previously been shown to bind to β-catenin and other molecules contained within key signaling nodes (16), suggesting a potentially important biological significance of IQGAP binding with TβRII.

IQGAP1 suppresses TGF-β1–mediated activation of pericytes into myofibroblasts. Since receptor stability and trafficking importantly regulate signaling, we tested the significance of IQGAP1/TβRII binding on myofibroblastic activation of HSCs. Two different siRNAs (QIAGEN) were used to knock down IQGAP1 of HSCs. Cells were stimulated with TGF-β1 (5 ng/ml) or PDGF-BB (20 ng/ml) and myofibroblastic activation of HSCs was assessed by WB for α-SMA, fibronectin, and phospho-SMAD2 (p-SMAD2). TGF-β1 more prominently activated HSCs as compared with PDGF-BB, as determined by upregulation of α-SMA, fibronectin, and p-SMAD2 (Figure 3A). IQGAP1 knockdown by 2 distinct IQGAP1 siRNAs also consistently potentiated TGF-β1 activation of HSCs (Figure 3A).

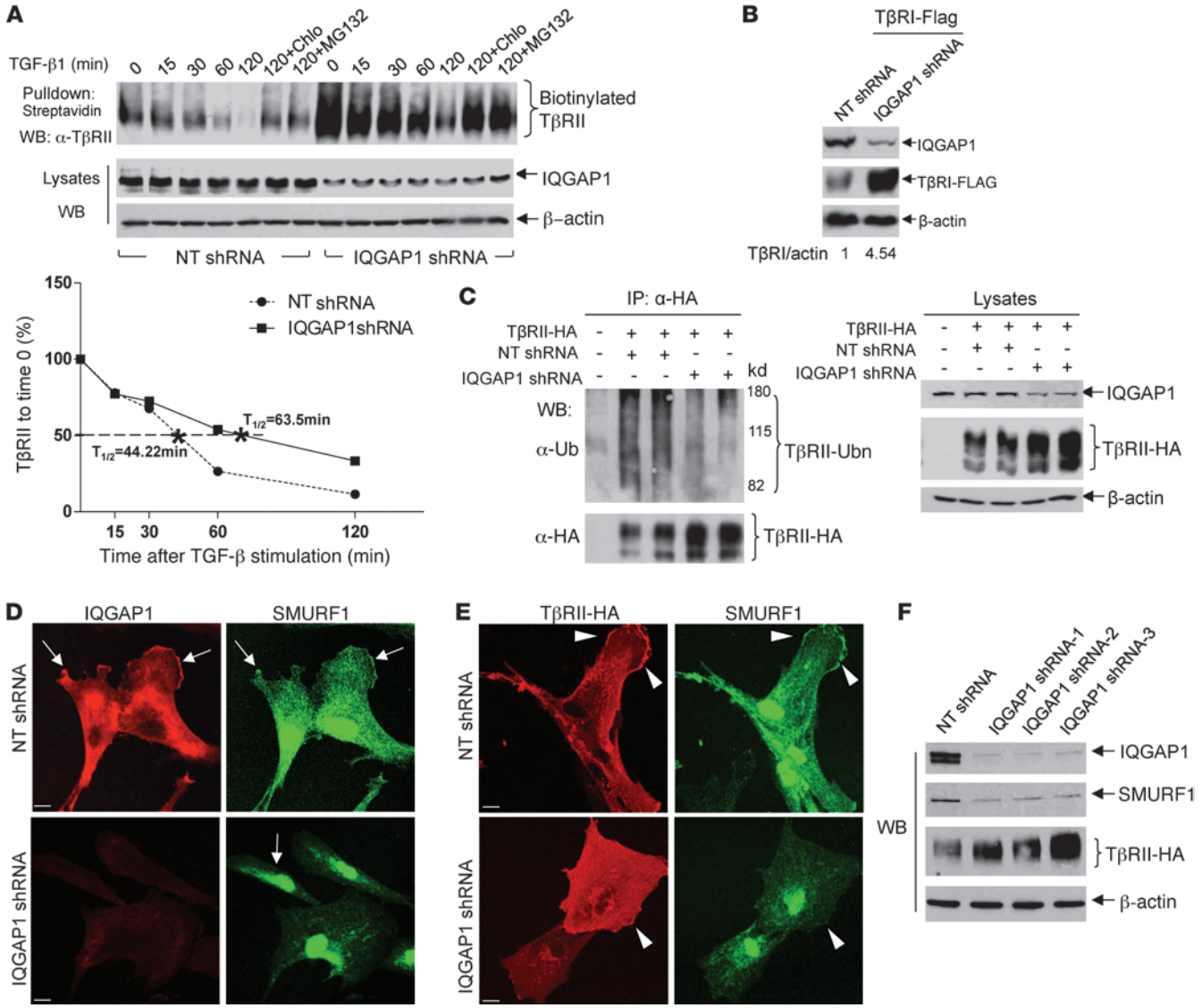

Figure 5

IQGAP1 knockdown inhibits TGF-β1 downregulation of TβRII, TβRII ubiquitination, and the plasma membrane targeting of SMURF1. (**A**) Top: HSCs with their cell-surface proteins prelabeled with biotin were incubated with TGF-1 for indicated times and cells were harvested for streptavidin pull-down and TβRII WB to determine internalized TβRII. Bottom: TβRII degradation curves generated by densitometric analysis are shown. IQGAP1 knockdown inhibited TGF-β1 downregulation of cell surface TβRII. Chlo, chloroquine; $T_{½}$, half-life of TβRII. Data are representative of multiple independent experiments. Asterisks designate a point where TβRII was down to 50%. (**B**) HSCs expressing TβRI-FLAG were transduced with lentiviruses encoding either NT shRNA or IQGAP1 shRNA, and TβRI protein levels were detected by Flag WB. IQGAP1 knockdown increased TβRI-Flag in HSCs. $n = 3$ experiments with similar results. (**C**) TβRII-HA was precipitated from HSCs by IP using anti-HA; TβRII ubiquitination was detected by WB. IQGAP1 knockdown markedly inhibited TβRII ubiquitination. (**D**) Double IF for IQGAP1 (red) and SMURF1 (green) revealed that IQGAP1 and SMURF1 colocalized at the periphery plasma membrane in control cells (arrows, upper panels), and that IQGAP1 knockdown reduced the localization of SMURF1 at the plasma membrane (lower panels). Scale bar: 20 μm. (**E**) TβRII and SMURF1 colocalized at the peripheral plasma membrane (arrowheads, upper panels), and IQGAP1 knockdown reduced TβRII/SMURF1 colocalization at the plasma membrane (lower panels). Scale bar: 20 μm. (**F**) IQGAP1 knockdown reduced SMURF1 protein levels in HSCs by WB. β-actin WB was used as a loading control. $n = 3$ independent experiments with identical results.

Double IF for IQGAP1 and α-SMA demonstrated that IQGAP1-knockdown cells exhibited prominent α-SMA–positive stress fibers, indicative of myofibroblastic transdifferentiation (arrows, Figure 3B). Quantitative data from cells stimulated with TGF-β1 revealed that IQGAP1 siRNA increased TGF-β1–induced myofibroblastic activation by 35% (Figure 3C). Moreover, a SMAD siRNA targeting both SMAD2 and SMAD3 abolished the effect of IQGAP1 siRNA on myofibroblastic activation (Supplemental Figure 3). As expected, overexpression of full-length IQGAP1 suppressed HSC activation and the IQGAP1 (1-1502) mutant failed to repress HSC activation (Figure 3D). Taken together, these data demonstrate that by binding to TβRII, IQGAP1 suppresses TGF-β1/SMAD–mediated myofibroblastic activation of HSCs in vitro.

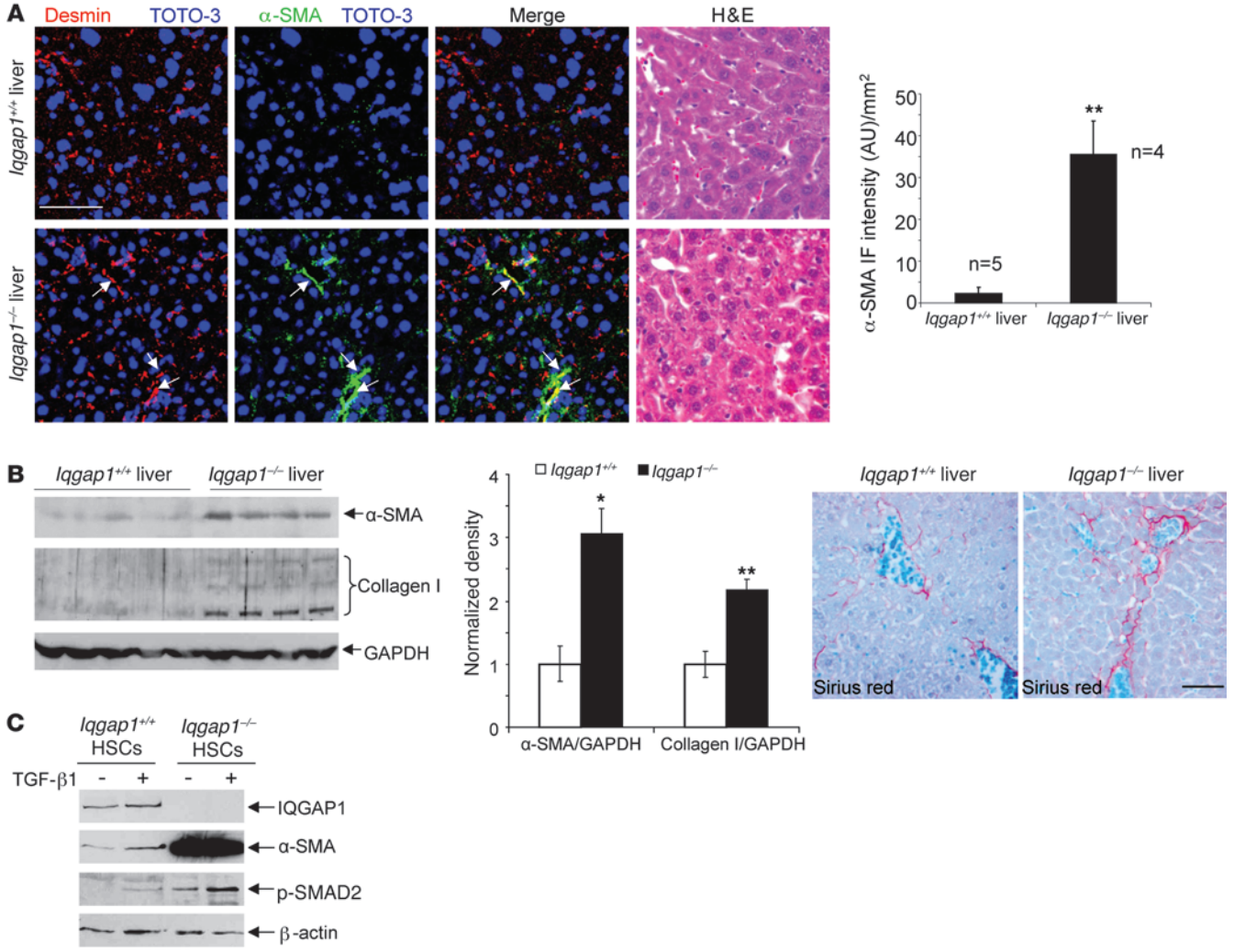

Figure 6

Basal activation phenotype of HSCs of *Iqgap1*$^{-/-}$ mice. (**A**) Left: livers of 1-year-old *Iqgap1*$^{-/-}$ and matched *Iqgap1*$^{+/+}$ mice were subjected to H&E staining, and double IF for desmin (red, HSC marker) and α-SMA (green, marker of activated HSCs). Cell nuclei were counterstained by TOTO-3 (blue). Arrows indicate colocalization of these 2 proteins. Scale bar: 50 μm. Right: quantitative data analyzed by ImageJ software revealed that α-SMA–positive HSCs were significantly increased in *Iqgap1*$^{-/-}$ livers compared with *Iqgap1*$^{+/+}$ livers. $^{**}P < 0.01$ by *t* test. (**B**) Left: liver samples as described in **A** were analyzed by WB for α-SMA and collagen I. Middle: densitometric analysis revealed that the average level of α-SMA or collagen I of *Iqgap1*$^{-/-}$ livers was significantly higher than that of *Iqgap1*$^{+/+}$ livers. $^{*}P < 0.05$; $^{**}P < 0.01$ by ANOVA. Right: representative images of Sirius red staining are shown. Scale bar: 50 μm. (**C**) HSCs of mice were treated with TGF-β1 at 72 hours after isolation and harvested for WB. *Iqgap1*$^{-/-}$ HSCs exhibited an enhanced activation phenotype as compared with *Iqgap1*$^{+/+}$ HSCs in vitro. *n* = 2 independent cell preparations using 4 mouse livers for each prep with similar results from both cell preparations.

TGF-β1 stimulation increases IQGAP1/TβRII binding. TGF-β1 ligand induces internalization and downregulation of TβRII (24–29). Therefore, we tested the hypothesis that IQGAP1 may modulate ligand-dependent internalization and degradation of TβRII in HSCs. To this end, we performed IP using anti-IQGAP1 and TβRII WB to detect TβRII/IQGAP1 binding. As shown in Figure 4A, TGF-β1 induced temporal increase of IQGAP1/TβRII binding, supporting a model whereby TGF-β1 stimulation recruits IQGAP1 to TβRII-containing signaling complexes, and in turn, IQGAP1 may modulate TβRII trafficking, degradation, and TGF-β1 signaling.

IQGAP1 knockdown inhibits lysosomal targeting of TβRII and induces accumulation of TβRII in the early endosomes. TβRII was localized to endosomes and its degradation was attenuated by lysosomal inhibitors (27, 28, 30–35), so we tested to determine whether IQGAP1 knockdown could alter the trafficking of TβRII to endosomes and lysosomes, 2 intracellular compartments where signaling and receptor turnover are regulated (31, 28, 34). HSCs treated with TGF-β1 were subjected to double IF for HA-tagged TβRII and lysosomal-associated membrane protein 1 (LAMP1, late endosome/lysosomal marker) or early endosome antigen 1 (EEA-1, early endosomal marker). IQGAP1 IF confirmed IQGAP1 knockdown in HSCs (Supplemental Figure 4A). Double IF revealed that at both 30 and 60 minutes after TGF-β1 stimulation, IQGAP1 knockdown significantly reduced TβRII reaching LAMP1-positive vesicles (late

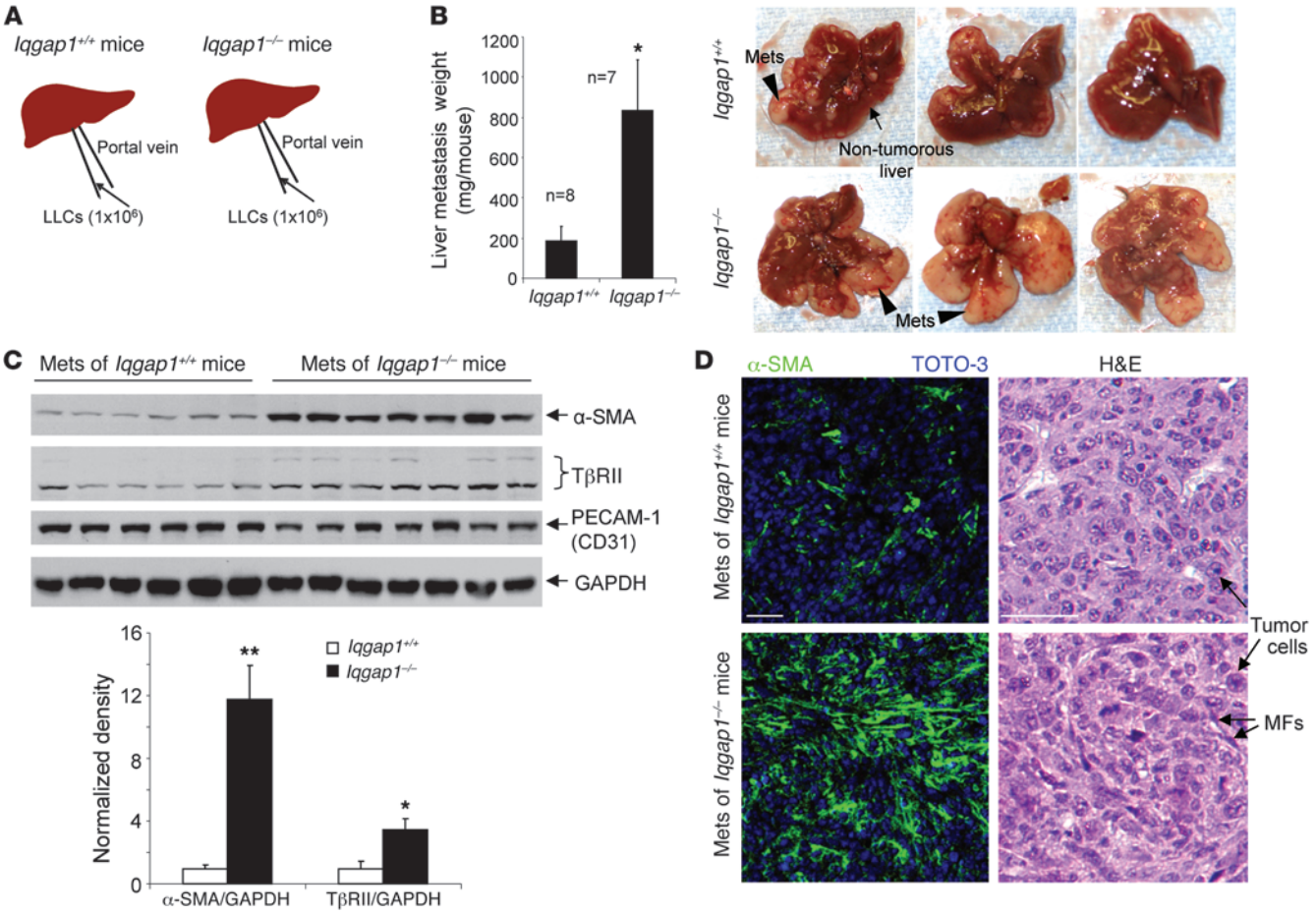

Figure 7

IQGAP1 deficiency in the liver promotes myofibroblastic activation and lung liver metastases in mice. (**A**) Depiction of portal vein implantation of LLCs into the livers of mice. (**B**) Left: average tumor weight of *Iqgap1*$^{-/-}$ livers was significantly higher than that of *Iqgap1*$^{+/+}$ livers at 10 days after tumor implantation. *$P < 0.05$ by *t* test. Right: representative photographs of liver and liver metastases (mets) of mice are shown. (**C**) WB on isolated liver metastases revealed that the average level of α-SMA or TβRII of the liver metastases of *Iqgap1*$^{-/-}$ mice was significantly higher than that of *Iqgap1*$^{+/+}$ mice. GAPDH WB was used as a protein loading control. *$P < 0.05$; **$P < 0.01$ by ANOVA. (**D**) Representative images of α-SMA IF (green) and H&E staining revealing more tumor-associated myofibroblasts in the liver metastases of *Iqgap1*$^{-/-}$ mice as compared with *Iqgap1*$^{+/+}$ mice. Cell nuclei were counterstained by TOTO-3 (blue). MFs, tumor-associated myofibroblasts. Scale bar: 50 μM.

endosome/lysosomes) (arrowheads, Figure 4, B and C). In control cells, TβRII/EEA-1 colocalization increased at 5 minutes after TGF-β1 stimulation and decreased gradually thereafter (Figure 4, D and E). In IQGAP1-knockdown cells, however, TβRII/EEA-1 colocalization continuously increased at 30 or 60 minutes after TGF-β1 stimulation (Figure 4, D and E), suggesting that IQGAP1 knockdown induces accumulation of TβRII in the early endosomes.

IQGAP1 knockdown inhibits lysosomal and proteasomal degradation of TβRII. We next used biotinylation of cell-surface proteins to analyze TGF-β1 downregulation of cell-surface TβRII in control and IQGAP1-knockdown cells. In control cells, TGF-β1 downregulated cell-surface TβRII in a time-dependent manner; TβRII half-life was about 44 minutes (Figure 5A). In IQGAP1-knockdown cells, however, it increased to about 63 minutes (Figure 5A), consistent with the observation that IQGAP1 knockdown inhibited TGF-β1–mediated lysosomal targeting of TβRII. Additionally, both chloroquine (Chlo, lysosomal inhibitor) and MG132 (proteasomal inhibitor) were able to partially prevent TβRII downregulation (Figure 5A). Furthermore, IQGAP1 knockdown also inhibited TGF-β1 downregulation of total cellular TβRII protein in cells that were pretreated with cycloheximide (Supplemental Figure 4B). Thus, these data support a model that IQGAP1 binds to TβRII and promotes TGF-β1–mediated lysosomal and proteasomal degradation of TβRII.

IQGAP1 knockdown inhibits TβRII ubiquitination. Since TGF-β stimulation induces the formation of complexes that contain TβRII and TβRI (5, 6), we compared TβRI protein levels in control and IQGAP1-knockdown HSCs. Similar to TβRII, IQGAP1 knockdown also increased exogenously expressed TβRI-FLAG in HSCs (Figure 5B), further supporting the model whereby IQGAP1 is recruited to the TGF-β receptor complexes where it promotes the degradation of TGF-β receptors.

Ubiquitination is an important signal for plasma membrane receptor internalization, multivesicular body sorting, and degradation (36). TβRII is also subjected to ubiquitin modification similarly to TβRI (33, 37), so we tested to determine whether IQGAP1

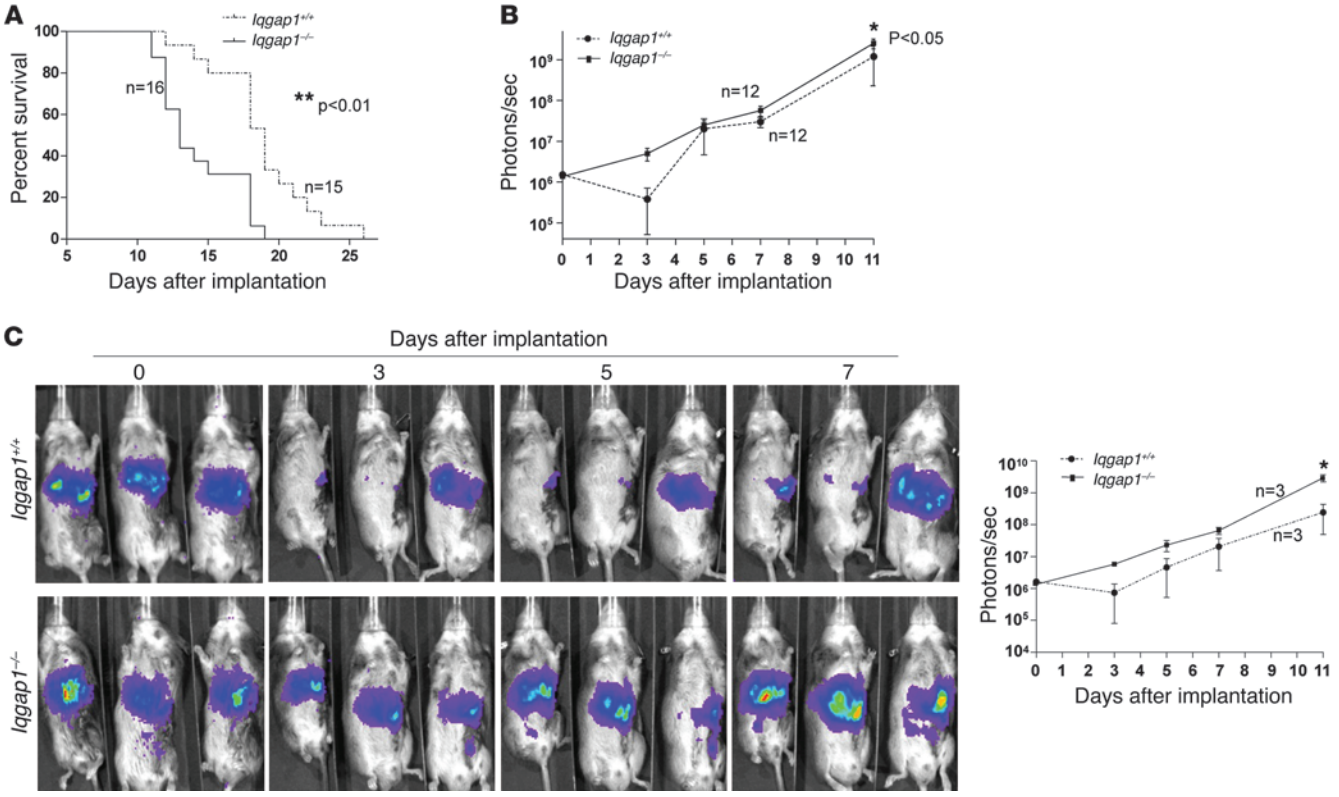

Figure 8

IQGAP1 deficiency in the liver promotes colorectal liver metastases in mice. (**A**) 2 × 10^6 MC38 mouse colorectal cancer cells were implanted into the livers of *Iqgap1*$^{-/-}$ and matched *Iqgap1*$^{+/+}$ mice by portal vein injection, and mouse survival was analyzed by GraphPad Prism 5 software. $^{**}P < 0.01$ by ANOVA. (**B** and **C**) MC38 cells tagged by firefly luciferase were injected into the livers of mice and bioluminescence of MC38 cells was quantitated by in vivo xenogen imaging at different days after tumor implantation. Data were analyzed by the GraphPad Prism 5 software, and representative images are shown. $^{*}P < 0.05$ by ANOVA.

knockdown influenced the ubiquitination of TβRII. To this end, TβRII-HA was precipitated from HSCs expressing TβRII-HA, and TβRII ubiquitination was detected by ubiquitin WB. As shown in Figure 5C, IQGAP1 knockdown markedly reduced the ubiquitination of TβRII in HSCs.

IQGAP1 is required for the targeting of SMURF1 to the plasma membrane. The turnover of TGF-β receptors is regulated by the E3 ubiquitin ligases such as SMURF1 and SMURF2, which interact and ubiquitinate TGF-β receptors at the plasma membrane (27, 38, 39). Based on this model, we tested to determine whether IQGAP1 knockdown influenced the subcellular localization of SMURF1. Consistent with the concept that SMURF1 localizes at the cellular protrusions (40), we found that in control HSCs, SMURF1 localized at the peripheral plasma membrane in addition to the nucleus and cytoplasm (arrows, Figure 5D). IQGAP1 knockdown reduced SMURF1 at the plasma membrane (Figure 5D) and SMURF1/TβRII colocalization at the plasma membrane (Figure 5E). Interestingly, we also found that IQGAP1 knockdown reduced the total protein levels of SMURF1 (Figure 5F), suggesting a role of IQGAP1 in the regulation of SMURF1 stability. Thus, IQGAP1 promotes the ubiquitination and degradation of TβRII in HSCs possibly by at least 2 different mechanisms: (a) directing SMURF1 to the plasma membrane where SMURF1 interacts with the TGF-β receptor complexes and (b) stabilizing SMURF1 protein levels.

Evidence for a basal activation phenotype of HSCs of Iqgap1$^{-/-}$ *mice*. To determine whether IQGAP1 suppresses HSC activation in vivo, we isolated livers from 1-year-old *Iqgap1*$^{+/+}$ and *Iqgap1*$^{-/-}$ mice for IF and WB. As compared with matched *Iqgap1*$^{+/+}$ livers, double IF revealed that *Iqgap1*$^{-/-}$ livers contained significantly more HSCs that were double-positive for α-SMA and desmin, another marker of HSCs (refs. 41, 42, and Figure 6A). WB confirmed this morphologic observation (Figure 6B). Additionally, *Iqgap1*$^{-/-}$ livers contained significantly more collagen I, as detected by WB (Figure 6B). Next, we isolated HSCs from mice and treated them with TGF-β1 for 24 hours and found that *Iqgap1*$^{-/-}$ HSCs exhibited an enhanced activation phenotype in vitro as compared with *Iqgap1*$^{+/+}$ HSCs (Figure 6C). Thus, these data support that IQGAP1 of HSCs suppresses HSC activation in vivo.

IQGAP1 deficiency in the tumor microenvironment promotes myofibroblastic activation and liver metastatic growth. The basal activation phenotype of HSCs of *Iqgap1*$^{-/-}$ mice led us to test if *Iqgap1*$^{-/-}$ livers promoted liver metastatic growth. Lewis lung carcinoma cells (LLCs), a mouse cancer cell line that is widely used in metastasis studies, were implanted into the livers of *Iqgap1*$^{+/+}$ and *Iqgap1*$^{-/-}$ mice by portal vein injection (Figure 7A). This study allowed us to study the specific effect of IQGAP1 depletion in the liver microenvironment on liver metastatic growth, since the implanted LLCs harbored intact IQGAP1 protein. Upon necropsy, we found

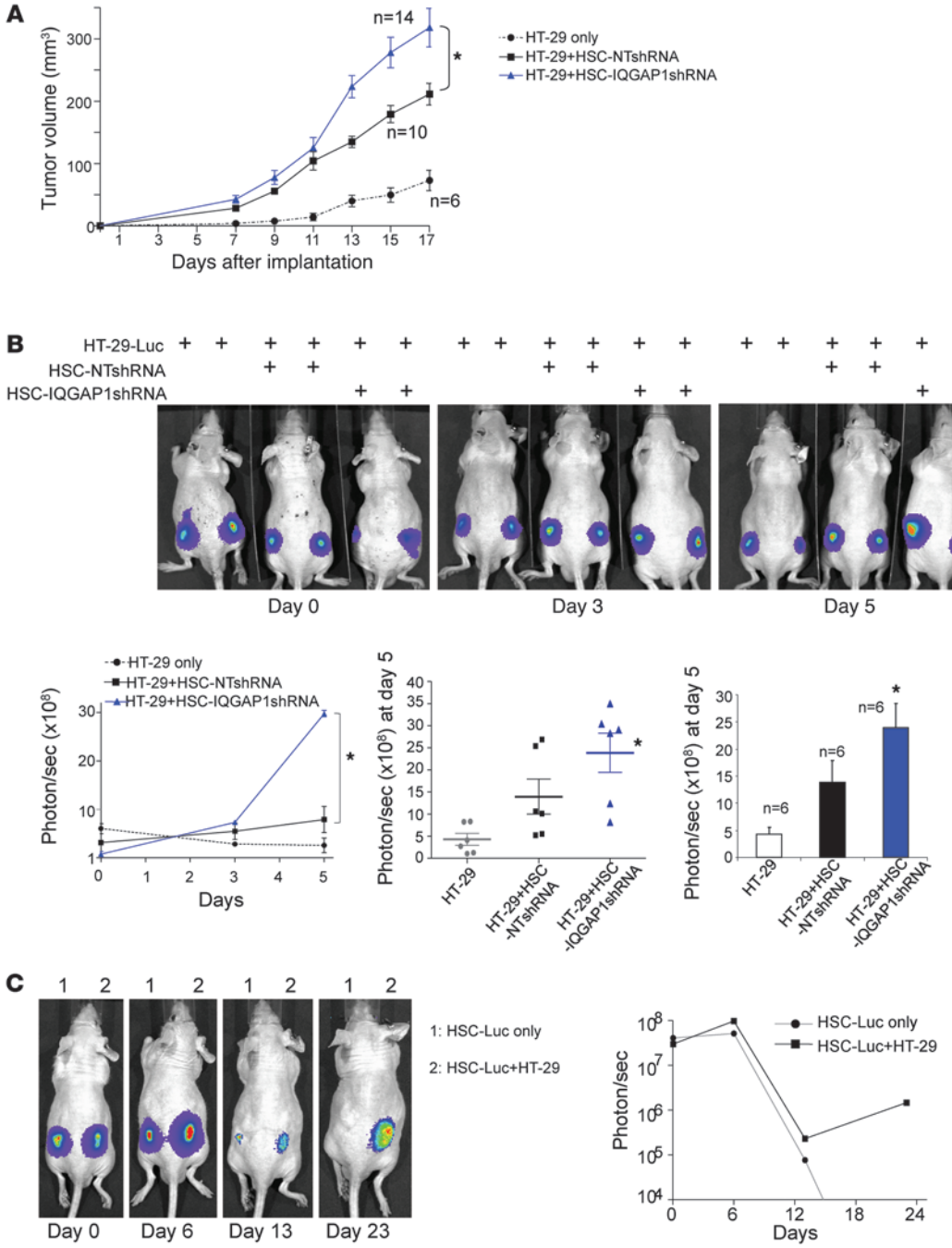

Figure 9

IQGAP1-knockdown HSCs promote colorectal tumor implantation and growth in HSC/tumor coimplantation model. (**A**) 0.5×10^6 HT-29 human colorectal tumor cells were mixed with 0.5×10^6 control HSCs (HSC-NTshRNA) or 0.5×10^6 IQGAP1-knockdown HSCs (HSC-IQGAP1shRNA), respectively, and coimplanted into nude mice via subcutaneous injection. Tumor nodules were measured by a caliper at different days after implantation, and data were analyzed by the GraphPad Prism 5 software. IQGAP1-knockdown HSCs exhibited a greater tumor-promoting effect as compared with control HSCs. *$P < 0.05$ by ANOVA. (**B**) 0.5×10^6 HT-29 cells tagged by firefly luciferase were mixed with 0.5×10^6 control HSCs or 0.5×10^6 IQGAP1-knockdown HSCs, respectively, and coimplanted into nude mice via subcutaneous injection. Bioluminescence of HT-29 cells was quantitated by in vivo xenogen imaging at indicated days after tumor implantation, and data were analyzed by GraphPad Prism 5 software. Imaging of representative mice and quantitative data are shown. IQGAP1-knockdown HSCs promoted the implantation of HT-29 cells in mice as compared with control HSCs. *$P < 0.05$ by ANOVA. (**C**) HSCs tagged by firefly luciferase were implanted into nude mice alone or with HT-29 tumor cells via subcutaneous injection. Bioluminescence of HSCs was quantitated by in vivo xenogen imaging at different days after implantation. Data are representative of 6 mice with consistent results. HSCs were able to survive up to 23 days in mice after HSC/tumor coimplantation.

that the average tumor weight in the liver of *Iqgap1*$^{-/-}$ mice was 4 times greater than that of *Iqgap1*$^{+/+}$ mice at 10 days after implantation (Figure 7B) (*Iqgap1*$^{+/+}$: 183.8 ± 72 mg/liver; *Iqgap1*$^{-/-}$: 832.7 ± 255 mg/liver; $P < 0.05$), indicating that IQGAP1 deficiency in the tumor microenvironment promotes liver metastatic growth in mice. Since *Iqgap1*$^{-/-}$ T cells do not exhibit reduced cytolytic function as compared with *Iqgap1*$^{+/+}$ T cells (43), this enhanced liver metastatic growth phenotype of *Iqgap1*$^{-/-}$ mice is unlikely to be due to IQGAP1 depletion in T cells.

Liver metastases isolated from the livers were subjected to WB and IF for α-SMA (maker of tumor-associated myofibroblasts) and PECAM-1/CD31 (marker of endothelial cells). As revealed by WB, the average level of α-SMA protein in the liver metastases of *Iqgap1*$^{-/-}$ mice was more than 10 times higher than that of *Iqgap1*$^{+/+}$ mice ($P < 0.01$) (Figure 7C). Consistent with our previously depicted in vitro data, the average level of TβRII protein in the liver metastases of *Iqgap1*$^{-/-}$ mice was more than 3 times higher than that of *Iqgap1*$^{+/+}$ mice ($P < 0.05$) (Figure 7C). In contrast, PECAM-1/CD31 protein levels were comparable in liver metastases of both groups (Figure 7C). IF confirmed that the liver metastases of *Iqgap1*$^{-/-}$ mice indeed contained more α-SMA–positive tumor-associated myofibroblasts (Figure 7D) and that endothelial cell densities were comparable in both groups (Supplemental Figure 6). Taken together, this liver metastasis study demonstrates that IQGAP1 in mesenchymal cells residing in the tumor microenvironment suppresses TβRII protein levels, myofibroblastic activation in vivo, and liver metastatic growth.

IQGAP1 deficiency in the tumor microenvironment promotes colorectal liver metastases. Since gastrointestinal cancers including colorectal and pancreatic cancers show a preference for liver metastasis, we next implanted MC38 mouse colorectal cancer cells into the livers of *Iqgap1*$^{+/+}$ and *Iqgap1*$^{-/-}$ mice. Similar to LLCs, MC38 cells implanted, quickly multiplied, and occupied mouse liver in vivo. The median survival of *Iqgap1*$^{+/+}$ mice was about 19 days, and it was shortened to 13 days for *Iqgap1*$^{-/-}$ mice ($P < 0.01$), confirming an enhanced colorectal liver metastatic growth phenotype in *Iqgap1*$^{-/-}$ mice (Figure 8A). Next, MC38 cells expressing firefly luciferase were implanted to determine whether IQGAP1 deficiency in the tumor microenvironment promoted tumor implantation into the liver. In vivo xenogen imaging that measured bioluminescence of MC38 cells revealed that at day 3 after tumor implantation, significantly more MC38 cells were detected in *Iqgap1*$^{-/-}$ livers than in *Iqgap1*$^{+/+}$ livers (Figure 8, B and C). These data indicate that *Iqgap1*$^{-/-}$ livers promote colorectal tumor implantation possibly by protecting the tumor cells from anoikis. This hypothesis was pursued as shown below.

IQGAP1-knockdown HSCs promote colorectal tumor implantation and growth in mice. In addition to HSCs, other liver-resident cells, such as fibroblasts, bone marrow–derived fibrocytes, hepatocytes, or cholangiocytes after epithelial-mesenchymal transition, are postulated to play a role in liver fibrosis (44). Therefore, we next performed an HSC/tumor cell coimplantation study to define a specific and selective role of HSCs for myofibroblastic activation and tumor growth. HT-29 human colorectal cancer cells that were mixed with an equal number of control HSCs (transduced with NT shRNA) or IQGAP1-knockdown HSCs (transduced with IQGAP1 shRNA) were implanted into nude mice via subcutaneous injection. Tumor growth curves generated by monitoring mice carefully for 17 days revealed that both control and IQGAP1-knockdown HSCs accelerated HT-29 tumor growth in mice (Figure 9A). Furthermore, IQGAP1-knockdown HSCs exerted a greater effect on promoting HT-29 tumor growth as compared with control HSCs (Figure 9A). Since HT-29 cells were tagged by firefly luciferase before implantation, in vivo xenogen imaging was performed to study the role of IQGAP1-knockdown HSCs in HT-29 implantation in mice (Figure 9B). At day 5 after implantation, the HT-29/HSC-IQGAP1 shRNA coimplantation group exhibited the highest level of HT-29 bioluminescence as compared with other groups (Figure 9B). A detailed analysis revealed that in the HT-29–only implantation group, HT-29 bioluminescence decreased continuously at days 3 and 5 after implantation, possibly representing anoikis of HT-29 cells, and that coimplantation of either control or IQGAP1-knockdown HSCs increased HT-29 bioluminescence at these time points (Figure 9B). Furthermore, coimplantation of IQGAP1-knockdown HSCs resulted in the greatest increase of HT-29 bioluminescence (Figure 9B). Thus, this HSC/tumor cell coimplantation study supports the concept that IQGAP1-knockdown HSCs promote colorectal tumor growth by promoting the implantation of tumor cells in mice.

IQGAP1 knockdown in HSCs promotes TβRII protein levels and myofibroblastic activation of HSCs in mice. To understand whether coimplanted HSCs indeed transdifferentiated into tumor-associated myofibroblasts in mice, we performed in vivo xenogen imaging to determine the survival of the coimplanted HSCs. HSCs tagged with firefly luciferase were implanted into nude mice alone (control) or with HT-29 cells via subcutaneous injection. In the HSC-only implantation group, bioluminescence of HSCs started to decrease continuously at day 6 to an undetectable level at day 14 after implantation (Figure 9C). In the HSC/tumor cell coimplantation group, however, it increased again at day 13 and remained at a detectable level at day 23 after implantation (Figure 9C; data are representative of 6 mice with consistent results). These data indicate that HSCs are able to survive up to 23 days after HSC/tumor cell coimplantation and that this prolonged survival of HSCs is dependent on tumor cells. Since the coimplanted HSCs were also tagged by TβRII-HA fusion proteins, we performed double IF on isolated tumor nodules to visualize the coimplanted HSCs. As revealed by double IF for HA tag and α-SMA, most HA-positive cells in the tumor nodules also expressed α-SMA (arrows, Figure 10A), suggesting that these coimplanted HSCs indeed transformed into tumor-associated myofibroblasts. WB revealed that the average level of TβRII-HA or α-SMA in tumors arising from IQGAP1-knockdown HSC coimplantation was significantly higher than that in tumors arising from control HSC coimplantation (Figure 10B). This finding was confirmed by IF for HA (Figure 10C) and α-SMA as well (Figure 10D). Thus, this HSC/tumor cell coimplantation study demonstrates a suppressive role of HSC IQGAP1 for TβRII protein, myofibroblastic activation, and tumor growth in vivo.

HSCs are activated into tumor-associated myofibroblasts of liver metastases. To determine whether HSCs in the liver indeed transdifferentiate into the tumor-associated myofibroblasts of liver metastases, we performed portal vein implantation of L3.6 human gastrointestinal cancer cells into the liver of SCID mice and isolated xenografts for IF. Stem121 is an antibody that has been extensively used to detect the engraftment of human cells transplanted into mice owing to its ability to detect a cytoplasmic protein specific to human origin cells. Double IF for α-SMA and Stem121 revealed that the stroma (S) of liver metastases identified by α-SMA–positive staining were negative for Stem121 and that tumor cells (T) were positive for Stem121 and negative for α-SMA (Figure 11A). These data indicate that these tumor-associated myofibroblasts were not derived from the implanted human cancer cells, but rather,

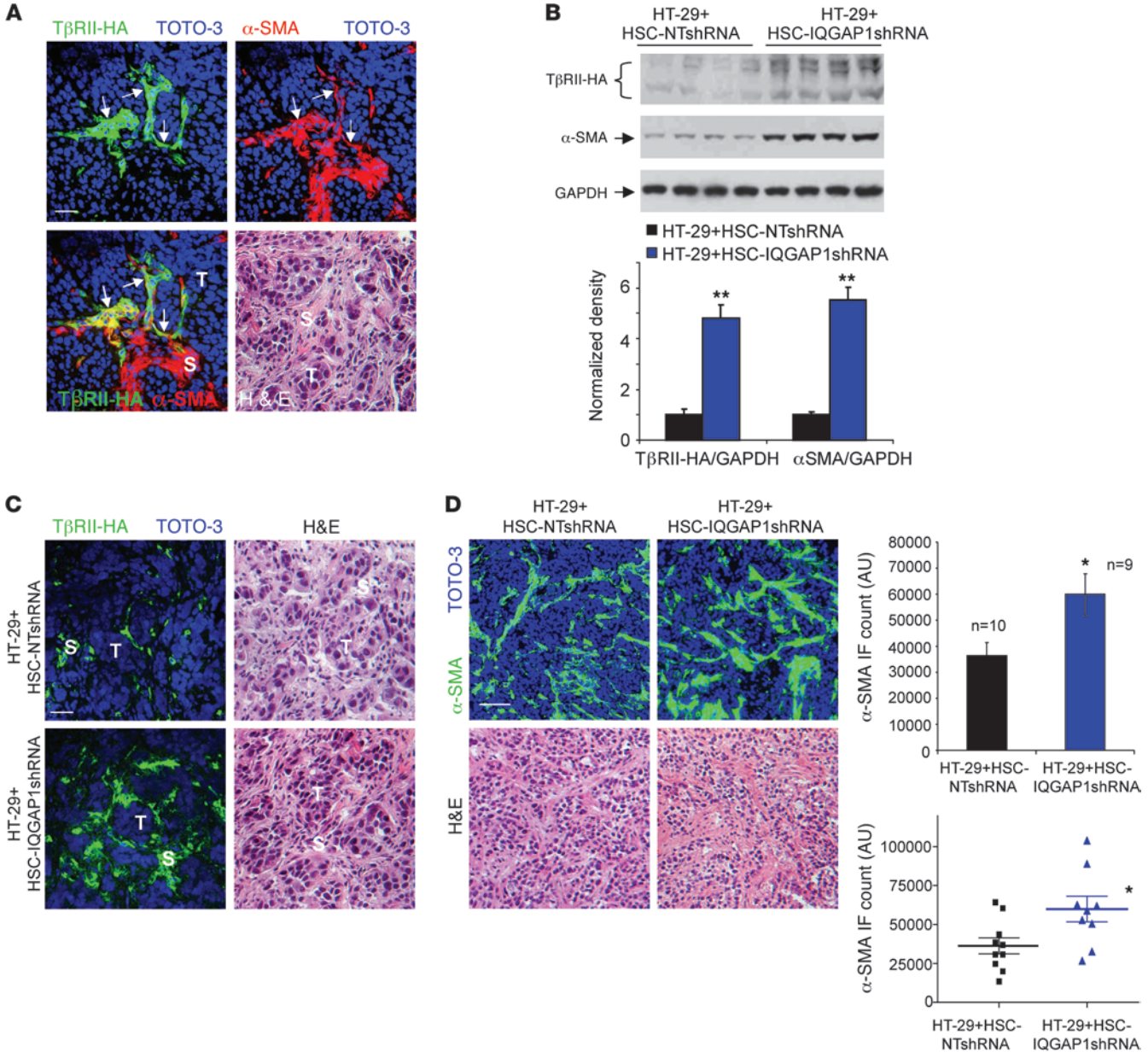

Figure 10

IQGAP1 knockdown in HSCs promotes TβRII levels, myofibroblastic activation of HSCs in a HSC/tumor coimplantation model. (**A**) HSCs expressing TβRII-HA were mixed with HT-29 tumor cells and coimplanted into nude mice via subcutaneous injection. Tumor nodules were subjected to IF for HA (green) and α-SMA (red) and H&E staining. Cells positive for both HA and α-SMA were detected in the tumor nodules (arrows). Cell nuclei were counterstained by TOTO-3 (blue). S, stroma; T, tumor cells. Scale bar: 50 μm. (**B**) Tumor nodules were subjected to WB and densitometric analysis. The average level of TβRII-HA or α-SMA in tumors arising from HT-29/HSC-IQGAP1shRNA coimplantation was significantly higher than that in tumors arising from HT-29/HSC-NTshRNA coimplantation. $^{**}P < 0.01$ by ANOVA. (**C**) Representative HA IF (green) and H&E staining revealing more TβRII-HA–positive tumor-associated myofibroblasts in tumor nodules arising from HT-29/HSC-IQGAP1shRNA coimplantation as compared with tumors arising from HT-29/HSC-NTshRNA coimplantation. Cell nuclei were counterstained by TOTO-3 (blue). Scale bar: 50 μm. (**D**) Tumor nodules were subjected to α-SMA IF (green), H&E staining, and quantitative analysis. The average α-SMA IF density in tumors arising from HT-29/HSC-IQGAP1shRNA coimplantation was significantly higher than that in tumors from HT-29/HSC-NTshRNA coimplantation. $^{*}P < 0.05$ by *t* test. Scale bar: 100 μm.

from cells residing in the host mouse liver. To identify their origin, immunohistochemistry for α-SMA and desmin was perform on adjacent sections of the liver metastases. As shown in Figure 11B, some of these stromal cells were indeed positive for desmin, suggesting that they may have an HSC origin. To test this hypothesis further, we performed double IF for α-SMA and desmin on liver sections containing L3.6 micrometastases and found that a fraction of HSCs adjacent to the L3.6 tumor cells were positive for both α-SMA and desmin (arrowheads, Figure 11C). Additionally, these activated HSCs were negative for Stem121 (arrows, Figure 11D).

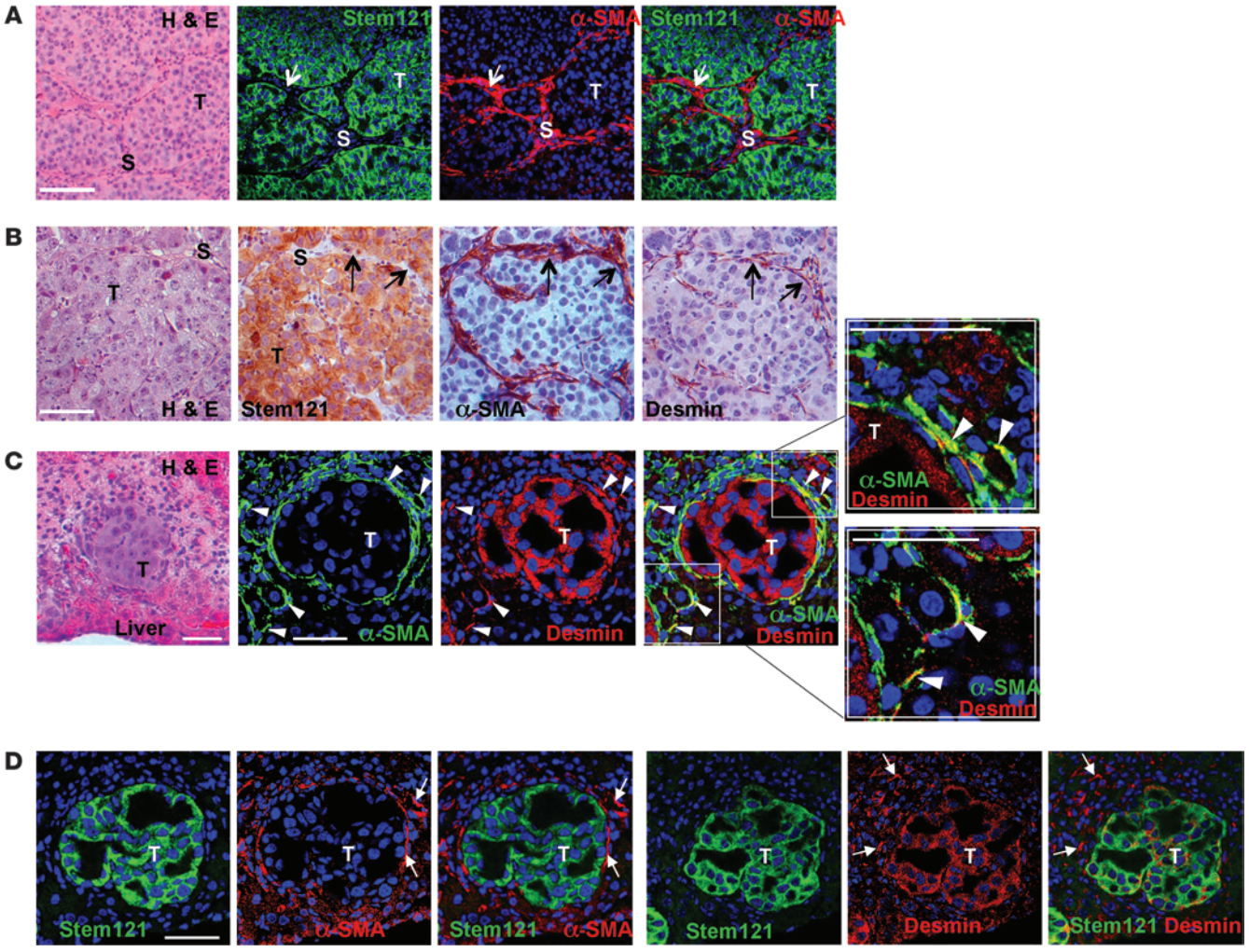

Figure 11
HSCs are activated into tumor-associated myofibroblasts of liver metastases. (**A**) L3.6 human gastrointestinal cancer cells were implanted into the livers of SCID mice by portal vein injection. Established liver metastases were isolated for H&E staining and double IF for Stem121 (green), a specific marker of human engraftments, and α-SMA (red). Tumor-associated myofibroblasts of liver metastases were negative for Stem121 (arrows). Cell nuclei were counterstained by TOTO-3 (blue). Scale bar: 100 μm. (**B**) Adjacent sections of L3.6 liver metastases were subjected to H&E staining, immunostaining for Stem121, α-SMA, or desmin. Some tumor-associated myofibroblasts were positive for desmin (arrows). Scale bar: 50 μm. (**C**) Liver sections containing L3.6 micrometastases were subjected to H&E staining and double IF for α-SMA (green) and desmin (red). Some HSCs at the sinusoids adjacent to L3.6 tumor cells were activated to express α-SMA (arrowheads). Cell nuclei were counterstained by TOTO-3 (blue). Scale bars: 50 μm. (**D**) Adjacent sections of micrometastases shown in **C** were subjected to double IF for Stem 121 and α-SMA or desmin. The activated HSCs adjacent to the tumor cells were negative for Stem 121 (arrows). Cell nuclei were counterstained by TOTO-3 (blue). Scale bar: 50 μm.

It is interesting that L3.6 cells were also positive for desmin, with desmin representing one of a panel of diagnostic markers for certain tumors (45, 46). Taken together, these data provide evidence for transactivation of liver-resident HSCs into the tumor-associated myofibroblasts using an experimental liver metastasis model.

IQGAP1-knockdown HSCs confer a greater stimulatory effect on proliferation, migration, and survival of tumor cells. To understand mechanisms by which IQGAP1-knockdown HSCs promoted liver metastatic growth in mice, conditioned medium were collected from control and IQGAP1-knockdown HSCs and incubated with tumor cells. MTS-based (with MTS indicating 3-[4,5-dimethylthiazol-2-yl]-5-[3-carboxymethoxyphenyl]-2-[4-sulfophenyl]-2H-tetrazolium, inner salt) nonradioactive cell proliferation assay and Boyden chamber assay were performed to test their effect on tumor cell proliferation and migration. As expected, the conditioned medium of control HSCs promoted the proliferation and migration of HT-29 (Figure 12, A and B) and LLCs (Supplemental Figure 7) as compared with basal medium. Importantly, the conditioned medium of IQGAP1-knockdown HSCs exhibited a greater stimulatory effect on tumor cells than that of control HSCs (Figure 12, A and B, and Supplemental Figure 7). As detected by DAPI staining and WB for PARP cleavage, an early marker of cell apoptosis, these conditioned media protected MC38 cells from apoptosis in cell suspension culture and anoikis assays, and the conditioned media of IQGAP1-knockdown HSCs conferred a greater protection to MC38 cells (Figure 12C). These data support

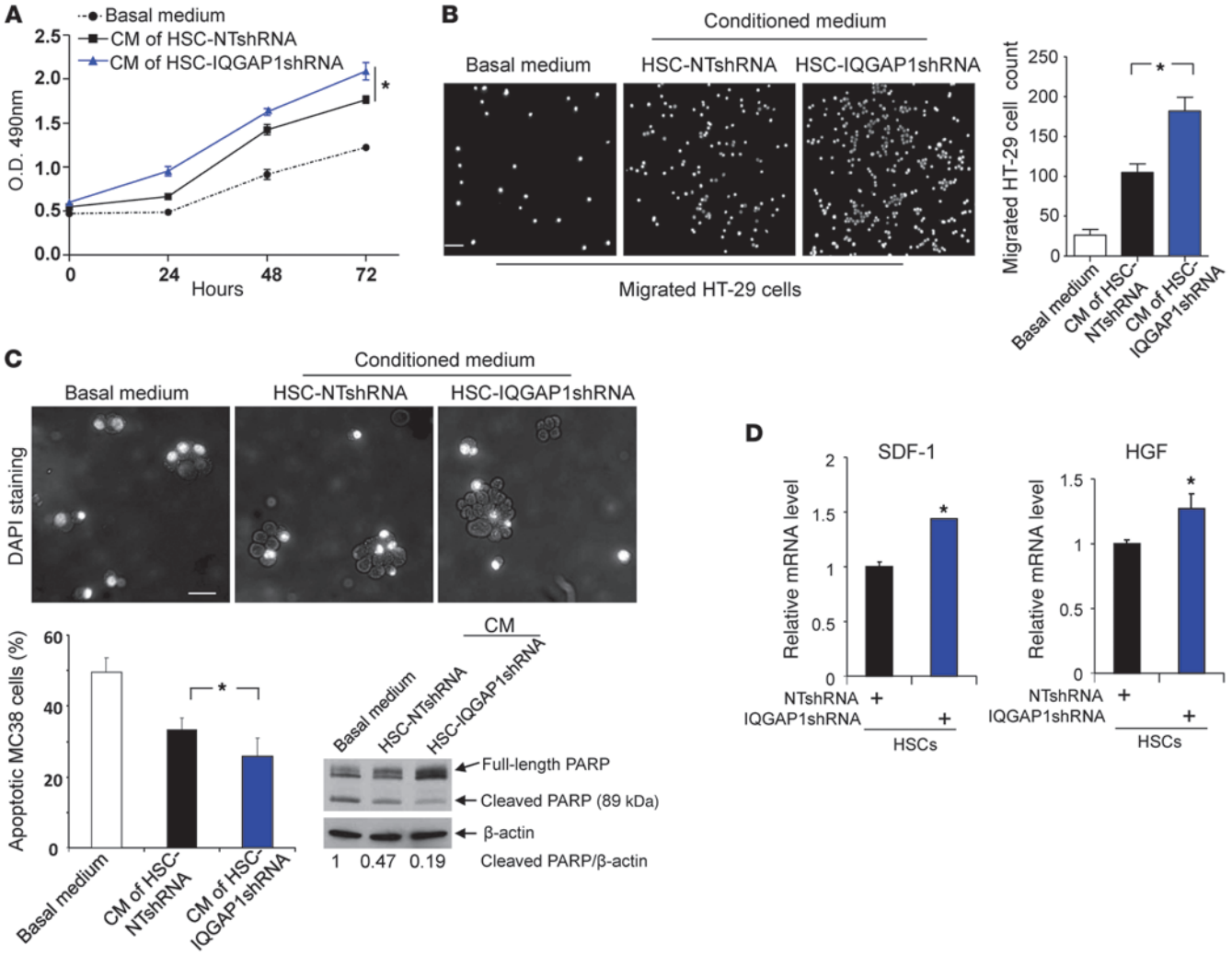

Figure 12

IQGAP1-knockdown HSCs promote the proliferation, migration, and survival of tumor cells. (**A**) Conditioned medium collected from control and IQGAP1-knockdown HSCs were used as a growth stimulant for HT-29 in nonradioactive cell proliferation assays. Conditioned medium of IQGAP1-knockdown HSCs promoted the proliferation of HT-29 cells as compared with that of control shRNA–transduced HSCs. CM, conditioned medium. *$P < 0.05$ by ANOVA; $n = 3$ repeats with similar results. (**B**) Conditioned medium collected as described in **A** were used as a chemoattractant for HT-29 in Boyden chamber assays. Conditioned medium of IQGAP1-knockdown HSCs promoted HT-29 migration as compared with that of control shRNA–transduced HSCs. *$P < 0.05$ by ANOVA; $n = 3$ repeats with similar results. Scale bar: 100 μm. (**C**) MC38 cells were suspended in basal medium or conditioned medium as described in **A** and seeded onto polyhydroxyethylmethacrylate (poly-HEMA) precoated culture dishes. After cells were incubated for 24 hours with gentle shaking, anoikis was assessed by DAPI staining of unfixed cells (top) and WB for PARP cleavage (lower right). Conditioned medium of IQGAP1-knockdown HSCs protected MC38 cells from anoikis as compared with that of control HSCs. *$P < 0.05$ by ANOVA. $n = 3$ repeats. Scale bar: 50 μm. (**D**) Control and IQGAP1-knockdown HSCs were harvested for RNA extraction and SYBR green–based real-time RT-PCR for SDF-1/CXCL12 and HGF. The mRNA level of SDF-1/CXCL12 or HGF was significantly increased by IQGAP1 knockdown in HSCs. *$P < 0.05$ by *t* test; $n = 3$ independent experiments.

that IQGAP1 deficiency in activated HSCs may confer a greater stimulatory effect on the growth and survival of tumor cells through the release of soluble factors.

Next, we isolated mRNAs from control and IQGAP1-knockdown HSCs for real-time quantitative RT-PCR analyses for paracrine cellular growth and motility factors, including TGF-β1, PDGF ligands, SDF-1/CXCL12, and HGF. Although the mRNA levels of TGF-β1 and PDGF ligands were not changed by IQGAP1 knockdown, the transcripts of SDF-1/CXCL12 and HGF were significantly increased by IQGAP1 knockdown in HSCs (Figure 12D). This finding is very interesting, since both SDF-1/CXCL12 and HGF play a central role in tumor metastasis and angiogenesis (47, 48) and SDF-1/CXCL12 has been identified as a chemokine that regulates organ-specific metastasis in various cancers (49–51).

IQGAP1 in the myofibroblasts of patient colorectal liver metastases is downregulated. Double IF for IQGAP1 and α-SMA was performed on liver biopsies of patients with colorectal cancers to determine IQGAP1 expression status in the stroma of established liver metastases. Liver biopsies of 29 colorectal cancer patients were obtained from a Mayo Clinic tissue collection. This patient cohort was 55% male and 45%

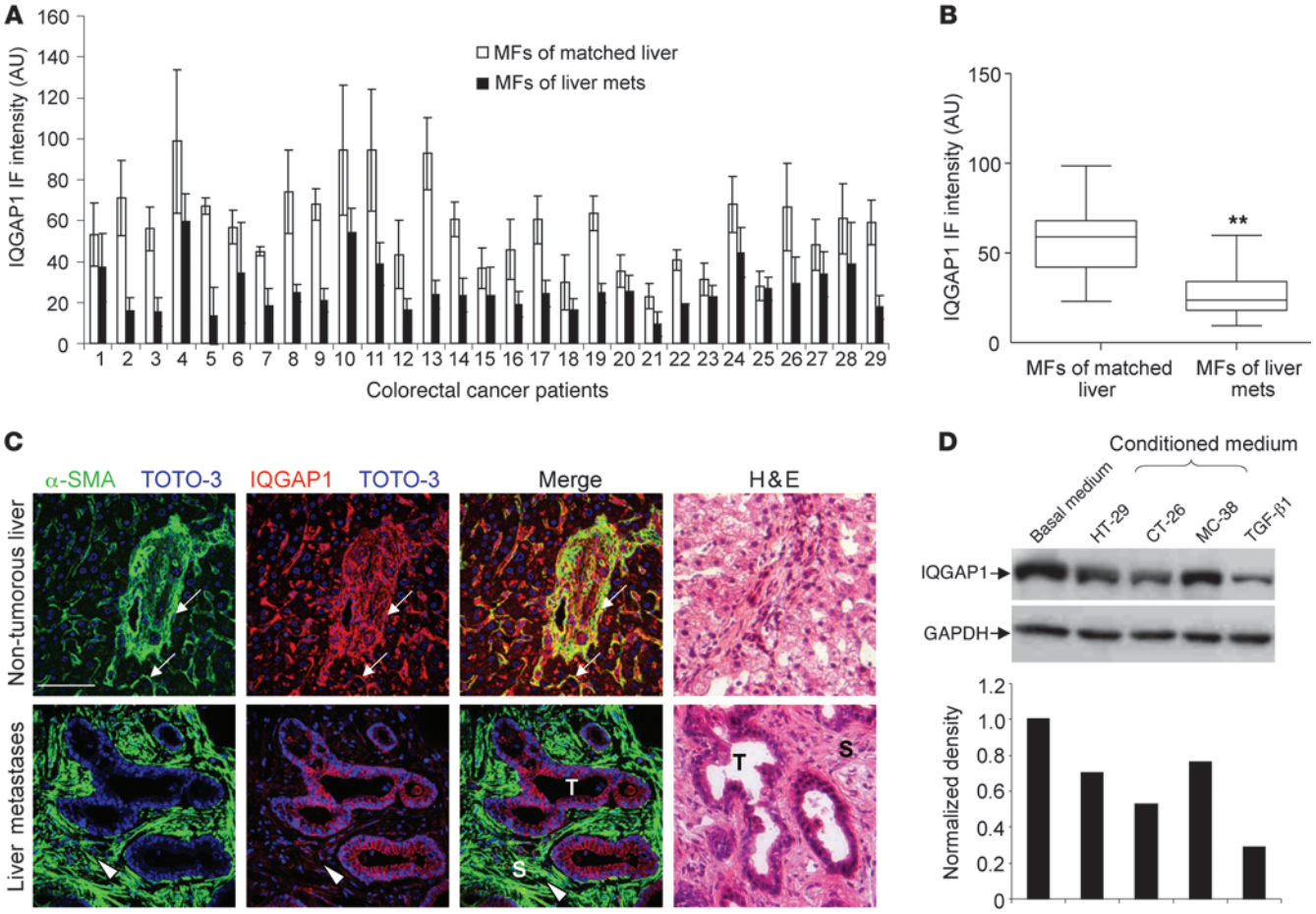

Figure 13

IQGAP1 in the myofibroblasts of human colorectal liver metastases is downregulated. (**A**) Double IF for IQGAP1 and α-SMA was performed on liver biopsies of 29 patients with metastatic colorectal cancer. IQGAP1 IF intensities in the myofibroblasts of liver metastases and matched control liver were quantitated by ImageJ software. MFs, myofibroblasts. (**B**) Box and whisker plots revealing that IQGAP1 in the myofibroblasts of patient colorectal liver metastases was significantly lower than that of the matched livers. $^{**}P < 0.01$ by *t* test. (**C**) IF and H&E staining of a representative patient are shown. Cell nuclei were counterstained by TOTO-3 (blue). Scale bar: 100 μm. (**D**) Conditioned media collected from HT-29, CT26, and MC38 colorectal cancer cells were incubated with HSCs for 24 hours. IQGAP1 protein levels of HSCs were determined by WB and densitometric analyses. Conditioned medium of colorectal tumor cells downregulated IQGAP1 of HSCs. TGF-β1 (5 ng/ml) recapitulated the effect of the conditioned medium. Data represent multiple experiments with similar results.

female, and all were clinically diagnosed with metastatic colorectal cancer (Supplemental Table 1). The age of patients was from 32 to 90 years old, with a median of 63 years old. Their primary colon cancers originated from different colonic sites including ascending, transverse, descending, sigmoid colon, and rectum. After double IF for α-SMA and IQGAP1, IQGAP1 IF intensity in the myofibroblasts of the liver metastases was quantitated and compared with that in the myofibroblasts of matched control liver (Figure 13, A–C, and Supplemental Table 1). Out of 29 patients analyzed, 24 patients displayed varying degrees of reduction of IQGAP1 protein in the myofibroblasts of their liver metastases as compared with IQGAP1 expression levels observed in activated HSCs and portal myofibroblasts of the adjacent nontumorous control liver (Figure 13, A and C). This reduction was statistically significant in this cohort as detected by Student's *t* test ($P < 0.01$) (Figure 13B).

Since metastatic growth in the liver is largely dependent on the communication between tumor cells and the hepatic tumor microenvironment, we next tested the hypothesis that when tumor cells intermingled with HSCs in the liver, tumor-derived factors might act on HSCs to reduce IQGAP1 expression of HSCs. To this end, conditioned medium of HT-29, MC38, and CT26 colorectal cancer cells were used to treat HSCs. As detected by WB, each conditioned medium tested indeed moderately reduced the IQGAP1 level of HSCs as compared with basal culture medium (Figure 13D). Furthermore, TGF-β1 (5 ng/ml) recapitulated the effect of the conditioned medium (Figure 13D), while PDGF-BB (20 ng/ml) did not (Supplemental Figure 8). Interestingly, IQGAP1 does not couple with TβRII for degradation after TGF-β1 stimulation, as shown in Figure 5A and Supplemental Figure 4B, indicating that IQGAP1 is downregulated by TGF-β1 through an alternative mechanism. Thus, that tumor-derived factors induced downregulation of IQGAP1 in the tumor-associated myofibroblasts may be important for the initiation and growth characteristics of colorectal liver metastasis in patients.

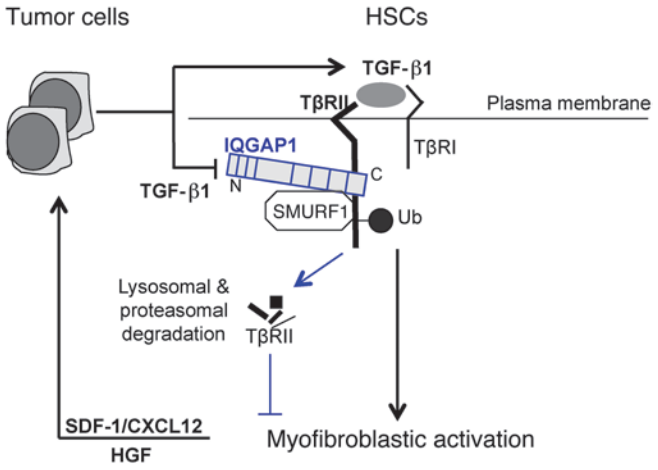

Figure 14
IQGAP1 of HSCs suppresses TGF-β activation of HSCs into myofibroblasts, and this effect is counterbalanced by tumor-derived factors. The C-terminal aa 1503–1657 of IQGAP1 binds to TβRII in a manner that is enhanced by TGF-β stimulation. IQGAP1 recruited to the TGF-β receptor complexes promotes SMURF1/TβRII colocalization at the plasma membrane, TβRII ubiquitination, and lysosomal and proteasomal degradation of TβRII. Thus IQGAP1 regulates TβRII degradation and cellular protein abundance. IQGAP1 binding and repression of TβRII suppresses activation of HSCs into myofibroblasts, thus limiting liver metastatic growth. Tumor-derived factors including TGF-β1, however, are able to downregulate IQGAP1 of HSCs, thereby amplifying the TGF-β1 activation of HSCs into tumor-associated myofibroblasts, which in turn, further promote liver metastatic growth by upregulating paracrine factors such as SDF-1/CXCL12 and HGF.

Discussion

Prior studies have demonstrated that IQGAP1 functions as an oncogenic protein in epithelial cells by virtue of its ability to interact with and modulate specific proteins with well-defined tumorigenic roles, such as Rac1, E-cadherin, β-catenin, EGF receptor and mTOR (7, 14, 15, 21). However, mice lacking IQGAP1 developed significantly more gastric hyperplasia and polyps at an older age (19). Interestingly, we demonstrate here that IQGAP1 suppresses the TGF-β1–mediated activation of HSCs into myofibroblasts in vitro and in vivo. IQGAP1 is recruited to TGF-β receptor complexes with the C-terminal aa 1503–1657 of IQGAP1 mediating IQGAP1/TβRII interaction (Figure 14). Through scaffolding TβRII and SMURF1, IQGAP1 promotes the ubiquitination and degradation of the TGF-β receptors, thus suppressing TβRII and the TGF-β1–mediated myofibroblastic transactivation of HSCs in the tumor microenvironment. Tumor-derived paracrine factors including TGF-β1, however, are able to partially remove this suppression of IQGAP1 by downregulating IQGAP1 of HSCs (Figure 14). Our study highlights bidirectional interactions between tumor cells and the tumor microenvironment for liver metastatic growth and supports an amplification loop whereby tumor cells downregulate HSC IQGAP and this in turn increases TGF-β1 signaling in HSCs that leads to transformation of HSCs into tumor-associated myofibroblasts. Tumor-associated myofibroblasts transdifferentiated from IQGAP1-deficient HSCs in turn further promote liver metastatic growth by upregulating paracrine cellular growth and motility factors such as SDF-1/CXCL12 and HGF (Figure 14).

During the evolution of cancer, tumor suppressor genes are often inactivated by various mechanisms, such as loss of heterozygosity, mutations, or epigenetic alterations (52). In this study, we found that IQGAP1 in the myofibroblasts of colorectal liver metastases is frequently downregulated in patients, akin to the well-characterized tumor suppressors in epithelial tumor cells. Mechanisms of such downregulation by tumor-derived paracrine factors including TGF-β1 are not well understood but may be a result of epigenetic changes. Our findings that IQGAP1 deficiency in HSCs promotes myofibroblastic activation and liver metastatic growth may be clinically important for human cancer, since they highlight the bidirectional interactions between tumor cells and HSCs, in particular the activated HSCs/myofibroblasts, as a potential therapeutic target for liver metastasis (2, 4). The activated HSCs are a rich source of growth factors and cytokines that promote tumor implantation, tumor angiogenesis, and tumor progression (4). Additionally, they regulate ECM turnover and suppress the antitumor immune response, creating a prometastatic microenvironment for tumor cells (4). Besides TGF-β, PDGF also activates HSCs by stimulating the proliferation and migration of HSCs/myofibroblasts. Imatinib mesylate (Gleevec), sunitinib, and sorafenib are recently approved anti-cancer drugs that target tyrosine kinases, such as the PDGF receptor, as well as intracellular kinases downstream from the TGF-β receptor, such as c-Abl (4, 23). Thus, these anti-cancer drugs and new compounds under development that are currently being tested in clinical trials may have implications in preventing and reducing liver metastases through the effect on the hepatic tumor microenvironment (2, 4).

SMURFs/SMAD7 complexes antagonize TGF-β signaling by at least 2 different mechanisms: (a) preventing TβRI-induced phosphorylation of receptor regulated Smads (R-Smads) by forming a complex with TβRI and (b) promoting the ubiquitination and degradation of TGF-β receptor complexes (27, 38). IQGAP1 is required for the targeting of SMURF1 to the peripheral plasma membrane where TβRII and SMURF1 colocalize, but we do not know if IQGAP1 binds to SMURF1 directly or not. Since SMAD7 recruits SMURF2 to the TGF-β receptors (27, 33), it is possible that IQGAP1 regulation of SMURF1 localization requires SMAD7. The accumulation of TβRII in the early endosomes of IQGAP1-knockdown cells suggests that IQGAP1 knockdown may block the sorting of TβRII from the early endosomes to late endosomal/lysosomal compartments for degradation. Alternatively, since TβRII is internalized via either clathrin-coated pits or clathrin-independent caveolar/lipid-raft (28), IQGAP1 knockdown may sequester TβRII from the caveolar/lipid-raft and thereby shift TβRII into the clathrin-dependent endocytic pathway, similar to a TβRII-trafficking model previously proposed (28, 32). Thus, while IQGAP has recently been implicated in exocytosis regulation (53), our study demonstrates what we believe is a new role for IQGAP1 in the regulation of endocytosis and degradation of receptors.

In summary, we demonstrate here a role for IQGAP1 in mesenchymal cells residing in the tumor microenvironment as compared with that previously described in epithelial cells, whereby IQGAP in the tumor microenvironment suppresses myofibroblastic activation and, in turn, is frequently downregulated in human colorectal liver metastases by the tumor-derived factors. Differentiation of roles of IQGAP1 in tumor cells and the tumor

stromal cells could help design better strategies to manipulate tumor cells, the tumor microenvironment, and tumor/stromal interactions in the process of tumor progression and metastasis. Furthermore, new and mechanistic information pertaining to the cell biological effects of IQGAP1 on TGF-β signaling should provide new insights relevant to a variety of diseases associated with desmoplasia and fibrosis.

Methods

Cell lines, expression vectors, and reagents. Human primary HSCs were purchased from ScienCell Research laboratories and cultured in DMEM supplemented with 10% fetal bovine serum and antibiotics (penicillin and streptomycin) (23, 54). HSCs with passage 5–10 were used in this study. LLCs and HT-29 human and CT26 mouse colon cancer cells were from ATCC. MC38 mouse colorectal cancer cells were provided by Steven A. Rosenberg (National Cancer Institute, Bethesda, Maryland, USA) and L3.6 cells were provided by Raul Urrutia (GI Research Unit, Mayo Clinic).

Retroviral vectors pMMP-TβRII-HA, pMMP-TβRI-FLAG, and pMMP-IQGAP1-YFP and lentiviral vectors expressing IQGAP1-FLAG or IQGAP1 (1-1502)-FLAG were generated by inserting a cDNA into pMMP or pSIN_BX-IRES lentiviral vector. All constructs were confirmed by sequencing and WB analysis. Retroviruses were generated and harvested by transfecting 293T cells with plasmids as previously described (55). Lentiviruses were generated by ViraPower Lentiviral Expression Systems (Invitrogen). Viral transduction was done by incubating cells with viral supernatant (25%) supplemented with polybrene (8 μg/ml) overnight at 37°C. Further experiments were performed at 48–96 hours after viral transduction.

hTGF-β1 was from R & D Systems (100-B). Antibodies used include anti-IQGAP1 (H-109) (sc-10792; Santa Cruz Biotechnology Inc.), anti-IQGAP1 (ab33542; Abcam), anti-TβRII (K105) (3713; Cell Signaling), anti-TβRII (E-6) (sc-17792; Santa Cruz Biotechnology Inc.), anti-EEA1 (610456; BD Transduction Laboratory), anti-LAMP1 (H4A3) (sc-20011; Santa Cruz Biotechnology Inc.), anti–α-SMA (A5228, Sigma-Aldrich), anti-fibronectin (610077; BD Transduction Laboratory), anti–p-SMAD2 (S465/467) (3101; Cell Signaling), anti-SMAD2/3 (3102; Cell Signaling), anti-HA (12CA5) (Roche Diagnostics), anti-HA (c29F4) (3724; Cell Signaling), anti-DYKDDDDK (FLAG tag) (2368; Cell Signaling), anti-ubiquitin (P4D1) (sc-8017; Santa Cruz Biotechnology Inc.), anti–PECAM-1/CD31 (M-20) (sc-1506; Santa Cruz Biotechnology Inc.), anti-PARP (556494; BD Biosciences — Pharmingen), anti-desmin (ab32362; Abcam), Stem121 antibody (AB-121; StemCells Inc.), anti-collagen I (600-401-103; Rockland), anti–β-actin (A5441; Sigma-Aldrich), and anti-GAPDH (G8140; US Biological).

Protein knockdown by shRNA or siRNA. Lentiviral vectors encoding distinct IQGAP1 shRNAs were purchased from Sigma-Aldrich (NM_003870.2-6211s1c1, NM_003870.2-3950s1c1, and NM_003870.2-569s1c1). Lentiviruses were generated by ViraPower Lentiviral Expression Systems (Invitrogen). SiRNAs were transfected into HSCs by Oligofectamine Reagent (Invitrogen). Control siRNA (SI03650318), IQGAP1 siRNA-1 (S100057043), IQGAP1 siRNA-2 (S100057050), IQGAP1 siRNA-3 (S102655268), and SMAD siRNA (S102757496) were from QIAGEN. All assays were performed at 72–96 hours after siRNA transfection.

IF, confocal microscopy, and quantification. HSCs that were fixed with 3% paraformaldehyde and permeabilized by 0.2% Triton X-100 were incubated with specific primary antibodies and Alexa Fluor–conjugated IgG (Invitrogen) was used for secondary detection. To stain mouse or human biopsies, frozen tissues were sectioned at 7 μm using a Leica cryostat. For double IF for TβRII and EEA-1 or LAMP1, HSCs that were serum starved and pretreated with cycloheximide (40 μg/ml) were incubated with TGF-β1 (5 ng/ml) at 4°C for 30 minutes for TGF-β1/receptor binding. Cells were then incubated at 37°C for various times before they were fixed with 2% formalin (in PIPE buffer, pH 6.95) (56). Fluorescence confocal images were captured by a LSM 5 Pascal Laser Scanning Microscope (Zeiss) using a ×63 or ×25 lens and Laser Scanning Microscope LSM PASCAL software (version 4.2 SP1).

To quantitate TβRII colocalization with EEA-1 or LAMP1, representative cells after IF were captured by a ×63 lens. After splitting merged pictures into single channels, the total number of vesicles positive for TβRII-HA in a cell was obtained by counting the vesicles that were green. The number of vesicles positive for both TβRII and EEA-1 or LAMP1 was obtained by counting vesicles that were yellow in merged pictures. The following equation was used: percentage of TβRII-HA colocalized with EEA-1 or LAMP1 = the number of yellow vesicles/the number of green vesicles × 100%. At least 6 representative cells per group were selected for analysis. To quantitate α-SMA IF on tissue sections, at least 3 microscopic fields per slide were selected randomly for analysis. Confocal images were converted to gray scale, and histograms were generated by ImageJ software (NIH). α-SMA IF counts were presented by the total frequencies of the gray and white pixels.

In situ cross-linking, IP, and WB analysis. In situ cross-linking was performed by incubating cells in 1 mM cross-linker dithiobis[succinimidylpropionate] (DSP) at room temperature for 30 minutes followed by 0.2 M glycine for 15 minutes to quench excess DSP. Cells were then harvested and lysed in a buffer containing 1% NP-40, 0.1% SDS, 0.25% deoxycholate acid, and protease inhibitors (Roche Diagnostics). Then, 1–2 μg antibody and 30 μl slurry of protein G–conjugated sepharose beads were used to pull down the protein complexes from HSC lysates (200–500 μg per sample). After beads were washed 4 times, precipitated proteins were eluted with Laemmli sample buffer (Bio-Rad) and loaded onto PAGE gels for WB. Immunoblotting was done as we previously described (55). Densitometry was performed by the ImageJ software (NIH).

GST pull-down and in vitro protein-binding assay. GST or GST fused truncated IQGAP1 proteins were purified from *E. coli* (BL21 DE3) by glutathione sepharose beads. GST pull-down assays were performed as described previously (57). For in vitro binding assays, the GST tag was first removed by thrombin, and detagged proteins were purified and recovered by the Thrombin Cleavage Capture Kit (Novagen, 69022). The detagged proteins were then incubated with GST alone or GST-fused proteins for binding assays as previously described (58).

Quantitation of TβRII degradation by biotinylation approach. Biotin labeling of cell-surface proteins and streptavidin-agarose pull-down were used to determine the degradation rate of cell surface TβRII by TGF-β1. In brief, serum-starved HSCs were cooled on ice to stop receptor endocytosis; biotin was then added into culture medium and incubated with cells at 4°C for 30 minutes (EZ-Link Sulfo-NHS-Biotin, 21217; Thermo Scientific). After free biotin was removed, TGF-β1 (final concentration is 5 ng/ml) was added and incubated with cells at 4°C for 30 minutes for TGF-β1/receptor binding. Cells were harvested after they were incubated at 37°C for various times. Streptavidin-agarose pull-down (S1638; Sigma-Aldrich) followed by WB for TβRII was used to quantitate TβRII that was internalized and spared from degradation.

Quantitative RT-PCR. Total RNA was extracted from HSCs using RNeasy kit (QIAGEN). Reverse transcription was performed using T15-oligonucleotide and Superscript RNase H-reverse transcriptase (Invitrogen). Amplification reactions were performed using a SYBR Green PCR Master Mix (Applied Biosystems) in an Applied Biosystems 7500 Real Time PCR System instrument. GAPDH was used in the same reaction of all samples as an internal control. mRNAs of interest were normalized to GAPDH mRNA and shown as the fold change. Primers were as follows: TβRII, TGTGTGACTTTGGGCTTTCC and GACATCGGTCTGCTTGAAGG; SDF-1/CXCL12, CCTTCCCTAACACTGGTT and TTGACCCGAAGCTAAAGTGG; HGF, CCCTGTAGCCTTCTCCTTGA and CGAGGCCATGGTGCTATACT.

Experimental liver metastasis and HSC/tumor cell coimplantation model. *Iqgap1*-knockout mouse line was generated by André Bernards (19) and maintained in 129/BL6 mixed background. Eight-week-old littermate *Iqgap1*$^{+/+}$ and *Iqgap1*$^{-/-}$ mice were used as recipients for the experimental liver metastasis study. Eight-week-old male SCID mice (01S11; Frederick National Lab) were also used as transplantation recipients. 1×10^6 LLCs, 1×10^6 L3.6 pancreatic cancer cells, or 2×10^6 MC38 mouse colorectal cancer cells were implanted into each mouse liver via portal vein injection as we previously described (55). Eight-week-old male nude mice (01B74; Frederick National Lab) were used as recipients for HSC/tumor cell coimplantation study. In brief, 0.5×10^6 HT-29 human colorectal cancer cells (50 μl in PBS) were mixed with 0.5×10^6 human HSCs with or without IQGAP1 knockdown (50 μl in PBS) and were coinjected into the lower flank of nude mice using a 0.5-cc syringe and a 27-gauge needle subcutaneously. Tumor diameters were measured by a caliper at different days after implantation. Tumor volume was calculated by the following formula: tumor volume = $(\text{width})^2 \times \text{length}/2$ (59).

In vivo xenogen imaging of mice. Cells expressing firefly luciferase were implanted into mice via portal vein injection or subcutaneous injection. On different days after tumor implantation, mice were injected with 150 μl D-luciferin (15 mg/ml) via intraperitoneal injection and anesthetized by isoflurane. In vivo xenogen imaging was performed using a Xenogen IVIS 200 machine (Caliper Life Sciences) and bioluminescence was quantitated using Living Image software (Caliper Life Sciences) (60).

Quantification of IQGAP1 expression in human colorectal liver metastases. Specimens containing liver metastases and matched peritumoral liver samples (control) were subjected to double IF for α-SMA and IQGAP1. IF confocal images were acquired by a LSM 5 Pascal Laser Scanning Microscope (Zeiss) using a ×25 lens. Two sets of images, one from liver metastasis regions and the other from matched liver, were taken from each patient for quantification using ImageJ software (NIH). In brief, regions of interest (ROIs) were chosen randomly at areas positive for α-SMA (rich in myofibroblasts) from the liver metastases and control liver, respectively, and integrated density (not affected by area) of IQGAP1 IF was calculated. More than 3 images were selected randomly from each section and at least 3 ROIs were chosen from each confocal image for analysis. The mean of multiple ROIs that were selected from a patient was calculated and data were exported to Microsoft Excel for further calculations. Finally, data generated from the liver metastases were compared with the matched control liver samples and a ratio was calculated for each patient.

Boyden chamber assay and cell proliferation assay. Conditioned medium was collected from serum-starved HSCs that were transduced with either NT shRNA or IQGAP1 shRNA. To assess the effect of the conditioned medium on tumor cell migration, 15,000 tumor cells were seeded into each upper well of a Boyden chamber (NeuroProbe). Basal medium and conditioned medium were used as chemoattractants in the bottom wells. Four hours later, cells that had migrated to the lower surface were stained with DAPI and cell images were captured from random microscopic fields by a fluorescence microscope. Cells were then counted by Metamorph software (Molecular Devices) (59). Cell proliferation assay was determined by a CellTiter 96 Aqueous Non-Radioactive Cell Proliferation Assay kit (Promega) according to the manufacturer's instruction. In brief, 2,500 cells that were suspended in 100 μl of conditioned medium were seeded into each well of a 96-culture plate. After cells were incubated at 37°C for different times, MTS and PMS reagents were added and cell numbers were presented by the absorbance at 490 nm using an ELISA plate reader.

Tumor cell anoikis assay. Tumor cell suspension culture and anoikis assays were performed as we described previously (55). In brief, 0.2×10^6 MC38 cells were seeded into a 6-well cell-culture dish coated with polyhydroxyethylmethacrylate (poly-HEMA) previously. Cells were then cultured in basal medium (control) or conditioned medium collected from control or IQGAP1-knockdown HSCs. Cells were cultured under a standard condition with gentle shaking for 24 hours. Apoptosis of cells was assessed by morphological analysis of cell nuclei DAPI staining (5 μg/ml) and by WB analysis for PARP cleavage, an early marker of cell apoptosis.

Statistics. All data are presented as mean ± SEM. Two-tailed Student's *t* test or ANOVA was used to evaluate statistical significance using GraphPad Prism 5 software (GraphPad Software, Inc). $P < 0.05$ was considered statistically significant.

Study approval. Animal protocols were approved by the Institutional Animal Care and Use Committee at the Mayo Clinic. Patient studies were approved by the Institutional Review Board at Mayo Clinic, and written informed consent was obtained from each patient.

Acknowledgments

We thank Kah Whye Peng and Yasuhiro Ikeda for providing reagents. The authors also acknowledge grant K01 CA118722, a 2009 Research Early Career Development Award (Mayo Clinic), the P/F Award and Clinical Core (P30 NIDDK 84567), and grants R01 CA160069 to N. Kang, R01 DK059615 to V.H. Shah, and; R01 NS051746 to G.S. Bloom.

Received for publication March 13, 2012, and accepted in revised form December 6, 2012.

Address correspondence to: Ningling Kang, Mayo Clinic, 200 First St SW, Rochester, Minnesota 55905, USA. Phone: 507.266.2840; Fax: 507.255.6318; E-mail: kang.ningling@mayo.edu.

1. Massague J. TGFbeta in cancer. *Cell*. 2008; 134(2):215–230.
2. Kalluri R, Zeisberg M. Fibroblasts in cancer. *Nat Rev Cancer*. 2006;6(5):392–401.
3. Shimoda M, Mellody KT, Orimo A. Carcinoma-associated fibroblasts are a rate-limiting determinant for tumour progression. *Semin Cell Dev Biol*. 2010;21(1):19–25.
4. Kang N, Gores GJ, Shah VH. Hepatic stellate cells: partners in crime for liver metastases? *Hepatology*. 2011;54(2):707–713.
5. Wrana JL, Attisano L, Wieser R, Ventura F, Massague J. Mechanism of activation of the TGF-beta receptor. *Nature*. 1994;370(6488):341–347.
6. Rahimi RA, Leof EB. TGF-beta signaling: a tale of two responses. *J Cell Biochem*. 2007;102(3):593–608.
7. White CD, Brown MD, Sacks DB. IQGAPs in cancer: A family of scaffold proteins underlying tumorigenesis. *FEBS Lett*. 2009;583(12):1817–1824.
8. Johnson M, Sharma M, Henderson BR. IQGAP1 regulation and roles in cancer. *Cell Signal*. 2009;21(10):1471–1478.
9. Noritake J, Watanabe T, Sato K, Wang S, Kaibuchi K. IQGAP1: a key regulator of adhesion and migration. *J Cell Sci*. 2005;118(pt 10):2085–2092.
10. White CD, Erdemir HH, Sacks DB. IQGAP1 and its binding proteins control diverse biological functions. *Cell Signal*. 2012;24(4):826–834.
11. Mateer SC, Wang N, Bloom GS. IQGAPs: integrators of the cytoskeleton, cell adhesion machinery, and signaling networks. *Cell Motil Cytoskeleton*. 2003;55(3):147–155.
12. Fukata M, et al. Rac1 and Cdc42 capture microtubules through IQGAP1 and CLIP-170. *Cell*. 2002;109(7):873–885.
13. Bensenor LB, et al. IQGAP1 regulates cell motility by linking growth factor signaling to actin assembly. *J Cell Sci*. 2007;120(pt 4):658–669.
14. Jadeski L, Mataraza JM, Jeong HW, Li Z, Sacks DB. IQGAP1 stimulates proliferation and enhances tumorigenesis of human breast epithelial cells. *J Biol Chem*. 2008;283(2):1008–1017.
15. Wang JB, Sonn R, Tekletsadik YK, Samorodnitsky D, Osman MA. IQGAP1 regulates cell proliferation through a novel CDC42-mTOR pathway. *J Cell Sci*. 2009;122(pt 12):2024–2033.
16. Kuroda S, et al. Role of IQGAP1, a target of the small GTPases Cdc42 and Rac1, in regulation of E-cadherin- mediated cell-cell adhesion. *Science*. 1998;281(5378):832–835.
17. Briggs MW, Li Z, Sacks DB. IQGAP1-mediated stimulation of transcriptional co-activation by beta-catenin is modulated by calmodulin. *J Biol Chem*. 2002;277(9):7453–7465.
18. Roy M, Li Z, Sacks DB. IQGAP1 is a scaffold for mitogen-activated protein kinase signaling. *Mol Cell Biol*. 2005;25(18):7940–7952.
19. Li S, Wang Q, Chakladar A, Bronson RT, Bernards A. Gastric hyperplasia in mice lacking the putative Cdc42 effector IQGAP1. *Mol Cell Biol*.

2000;20(2):697–701.
20. Yamaoka-Tojo M, et al. IQGAP1, a novel vascular endothelial growth factor receptor binding protein, is involved in reactive oxygen species--dependent endothelial migration and proliferation. *Circ Res*. 2004;95(3):276–283.
21. McNulty DE, Li Z, White CD, Sacks DB, Annan RS. MAPK scaffold IQGAP1 binds the EGF receptor and modulates its activation. *J Biol Chem*. 2011;286(17):15010–15021.
22. Vidal-Vanaclocha F. The prometastatic microenvironment of the liver. *Cancer Microenviron*. 2008;1(1):113–129.
23. Cao S, et al. Neuropilin-1 promotes cirrhosis of the rodent and human liver by enhancing PDGF/TGF-beta signaling in hepatic stellate cells. *J Clin Invest*. 2010;120(7):2379–2394.
24. Centrella M, Ji C, Casinghino S, McCarthy TL. Rapid flux in transforming growth factor-beta receptors on bone cells. *J Biol Chem*. 1996;271(31):18616–18622.
25. Koli KM, Arteaga CL. Processing of the transforming growth factor beta type I and II receptors. Biosynthesis and ligand-induced regulation. *J Biol Chem*. 1997;272(10):6423–6427.
26. Anders RA, Dore JJ Jr, Arline SL, Garamszegi N, Leof EB. Differential requirement for type I and type II transforming growth factor beta receptor kinase activity in ligand-mediated receptor endocytosis. *J Biol Chem*. 1998;273(36):23118–23125.
27. Kavsak P, et al. Smad7 binds to Smurf2 to form an E3 ubiquitin ligase that targets the TGF beta receptor for degradation. *Mol Cell*. 2000;6(6):1365–1375.
28. Di Guglielmo GM, Le Roy C, Goodfellow AF, Wrana JL. Distinct endocytic pathways regulate TGF-beta receptor signalling and turnover. *Nat Cell Biol*. 2003;5(5):410–421.
29. Mitchell H, Choudhury A, Pagano RE, Leof EB. Ligand-dependent and -independent transforming growth factor-beta receptor recycling regulated by clathrin-mediated endocytosis and Rab11. *Mol Biol Cell*. 2004;15(9):4166–4178.
30. Massague J, Kelly B. Internalization of transforming growth factor-beta and its receptor in BALB/c 3T3 fibroblasts. *J Cell Physiol*. 1986; 128(2):216–222.
31. Hayes S, Chawla A, Corvera S. TGF beta receptor internalization into EEA1-enriched early endosomes: role in signaling to Smad2. *J Cell Biol*. 2002;158(7):1239–1249.
32. McLean S, Di Guglielmo GM. TGF beta (transforming growth factor beta) receptor type III directs clathrin-mediated endocytosis of TGF beta receptor types I and II. *Biochem J*. 2010;429(1):137–145.
33. Atfi A, et al. The disintegrin and metalloproteinase ADAM12 contributes to TGF-beta signaling through interaction with the type II receptor. *J Cell Biol*. 2007;178(2):201–208.
34. Chen YG. Endocytic regulation of TGF-beta signaling. *Cell Res*. 2009;19(1):58–70.
35. Ehrlich M, Shmuely A, Henis YI. A single internalization signal from the di-leucine family is critical for constitutive endocytosis of the type II TGF-beta receptor. *J Cell Sci*. 2001;114(pt 9):1777–1786.
36. Haglund K, Sigismund S, Polo S, Szymkiewicz I, Di Fiore PP, Dikic I. Multiple monoubiquitination of RTKs is sufficient for their endocytosis and degradation. *Nat Cell Biol*. 2003;5(5):461–466.
37. Fukasawa H, et al. Reduction of transforming growth factor-beta type II receptor is caused by the enhanced ubiquitin-dependent degradation in human renal cell carcinoma. *Int J Cancer*. 2010;127(7):1517–1525.
38. Ebisawa T, et al. Smurf1 interacts with transforming growth factor-beta type I receptor through Smad7 and induces receptor degradation. *J Biol Chem*. 2001;276(16):12477–12480.
39. Suzuki C, et al. Smurf1 regulates the inhibitory activity of Smad7 by targeting Smad7 to the plasma membrane. *J Biol Chem*. 2002;277(42):39919–39925.
40. Wang HR, et al. Regulation of cell polarity and protrusion formation by targeting RhoA for degradation. *Science*. 2003;302(5651):1775–1779.
41. Niki T, De Bleser PJ, Xu G, Van Den Berg K, Wisse E, Geerts A. Comparison of glial fibrillary acidic protein and desmin staining in normal and CCl4-induced fibrotic rat livers. *Hepatology*. 1996;23(6):1538–1545.
42. Puche JE, et al. A novel murine model to deplete hepatic stellate cells uncovers their role in amplifying liver damage [published online ahead of print September 7, 2012]. *Hepatology*. doi:10.1002/hep.26053.
43. Gorman JA, et al. The cytoskeletal adaptor protein IQGAP1 regulates TCR-mediated signaling and filamentous actin dynamics. *J Immunol*. 2012;188(12):6135–6144.
44. Friedman SL. Evolving challenges in hepatic fibrosis. *Nat Rev Gastroenterol Hepatol*. 2010;7(8):425–436.
45. Ma Y, et al. Proteomics identification of desmin as a potential oncofetal diagnostic and prognostic biomarker in colorectal cancer. *Mol Cell Proteomics*. 2009;8(8):1878–1890.
46. Sugimoto T, et al. Alpha-smooth-muscle actin and desmin expressions in human neuroblastoma cell lines. International journal of cancer. *Int J Cancer*. 1991;48(2):277–283.
47. Gherardi E, Birchmeier W, Birchmeier C, Vande Woude G. Targeting MET in cancer: rationale and progress. Nature reviews. *Cancer*. 2012;12(2):89–103.
48. Domanska UM, et al. A review on CXCR4/CXCL12 axis in oncology: No place to hide [published online ahead of print June 8 2012]. *Eur J Cancer*. doi:10.1016/j.ejca.2012.05.005.
49. Muller A, et al. Involvement of chemokine receptors in breast cancer metastasis. *Nature*. 2001;410(6824):50–56.
50. Taichman RS, Cooper C, Keller ET, Pienta KJ, Taichman NS, McCauley LK. Use of the stromal cell-derived factor-1/CXCR4 pathway in prostate cancer metastasis to bone. *Cancer Res*. 2002;62(6):1832–1837.
51. Pan J, et al. Stromal derived factor-1 (SDF-1/CXCL12) and CXCR4 in renal cell carcinoma metastasis. *Mol Cancer*. 2006;5:56.
52. Nishida N, Goel A. Genetic and epigenetic signatures in human hepatocellular carcinoma: a systematic review. *Curr Genomics*. 2011;12(2):130–137.
53. Rittmeyer EN, Daniel S, Hsu SC, Osman MA. A dual role for IQGAP1 in regulating exocytosis. *J Cell Sci*. 2008;121(pt 3):391–403.
54. Semela D, Das A, Langer D, Kang N, Leof E, Shah V. Platelet-derived growth factor signaling through ephrin-b2 regulates hepatic vascular structure and function. *Gastroenterology*. 2008;135(2):671–679.
55. Decker NK, et al. Nitric oxide regulates tumor cell cross-talk with stromal cells in the tumor microenvironment of the liver. *Am J Pathol*. 2008;173(4):1002–1012.
56. Schroeder B, Weller SG, Chen J, Billadeau D, McNiven MA. A Dyn2-CIN85 complex mediates degradative traffic of the EGFR by regulation of late endosomal budding. *EMBO J*. 2010;29(18):3039–3053.
57. Cao S, et al. Direct interaction between eNOS and dynamin-2:Implications for NOS function. *J Biol Chem*. 2001;276(17):14249–14256.
58. Cao S, Yao J, Shah V. The proline rich domain of dynamin-2 is responsible for dynamin-dependent potentiation of eNOS activity via selective effects on reductase domain function. *J Biol Chem*. 2003;278(8):5894–5901.
59. Kang N, et al. Focal adhesion assembly in myofibroblasts fosters a microenvironment that promotes tumor growth. *Am J Pathol*. 2010;177(4):1888–1900.
60. Liu C, Russell SJ, Peng KW. Systemic therapy of disseminated myeloma in passively immunized mice using measles virus-infected cell carriers. *Mol Ther*. 2010;18(6):1155–1164.